BAMS Article

Why Do Eastern North Pacific Hurricanes Intensify More and Faster than Their Western-Counterpart Typhoons with Less Ocean Energy?

Il-Ju Moon, Thomas R. Knutson, Hye-Ji Kim, Alexander V. Babanin, and Jin-Yong Jeong

ABSTRACT: Tropical cyclones operate as heat engines, deriving energy from the thermodynamic disequilibrium between ocean surfaces and atmosphere. Available energy for the cyclones comes primarily from upper-ocean heat content. Here, we show that eastern North Pacific hurricanes reach a given intensity 15% faster on average than western North Pacific typhoons despite having half the available ocean heat content. Eastern North Pacific hurricanes also intensify on average 16% more with a given ocean energy (i.e., air–sea enthalpy flux) than western North Pacific typhoons. As efficient intensifiers, eastern Pacific hurricanes remain small during their intensification period, tend to stay at lower latitudes, and are affected by relatively lower vertical wind shear, a colder troposphere, and a drier boundary layer. Despite a shallower warm upper-ocean layer in the eastern North Pacific, average hurricane-induced sea surface cooling there is only slightly larger than in the western North Pacific due to the opposing influences of stronger density stratification, smaller size, and related wave-interaction effects. In contrast, western North Pacific typhoons encounter a more favorable oceanic environment for development, but several factors cause typhoons to greatly increase their size during intensification, resulting in a slow and inefficient intensification process. These findings on tropical cyclones' basin-dependent characteristics contribute toward a better understanding of TC intensification.

KEYWORDS: Mixing; Wind waves; Atmosphere-ocean interaction; Hurricanes/typhoons; Thermodynamics; Ocean models

https://doi.org/10.1175/BAMS-D-21-0131.1

Corresponding authors: Il-Ju Moon, ijmoon@jejunu.ac.kr; Hye-Ji Kim, hjkim@jejunu.ac.kr

In final form 22 July 2022

AFFILIATIONS: Moon and Kim—Typhoon Research Center, Jeju National University, Jeju, South Korea; **Knutson**—NOAA/Geophysical Fluid Dynamics Laboratory, Princeton, New Jersey; **Babanin**—University of Melbourne, Melbourne, Victoria, Australia; **Jeong**—Korea Institute of Ocean Science and Technology, Busan, South Korea

Tropical cyclones (TCs), which are rapidly rotating storm systems originating over tropical oceans, are one of the biggest threats to human life and property. The primary energy sources for TCs are warm ocean waters. High upper-ocean heat content (OHC), defined by the integrated internal energy from the surface to the depth of the 26°C isotherm, is a basic thermodynamical condition for TC intensification (except in rare circumstances, 26°C is the minimum surface temperature associated with TC development in the current climate; Leipper and Volgenau 1972; Tory and Dare 2015). OHC is known to be a very widely used oceanic predictor widely used in operational TC intensity forecasting (DeMaria et al. 2005; Mainelli et al. 2008; Moon and Kwon 2012). In particular, OHC can modulate the sea surface cooling effects (negative feedback on TC intensity) caused by wind-driven mixing of deeper cold water with the warm surface waters during the passage of a TC over the ocean (Kim et al. 2018; Lin et al. 2008; Shay et al. 2000; Wada and Usui 2007).

In general, the higher the OHC, the stronger the TC can become; however, the relationship between TC intensity and OHC is complex when comparing individual TC cases quantitatively. For example, consider two recent TCs of record-breaking intensity in the western North Pacific (WNP) and the eastern North Pacific (ENP): Typhoon Haiyan in 2013 and Hurricane Patricia in 2015. Typhoon Haiyan—the strongest landfalling TC on record—killed at least 6,300 people in the Philippines alone (Mori et al. 2014); Hurricane Patricia—the most intense and rapidly intensifying TC ever observed in the Western Hemisphere—caused extensive damage in Mexico (Kimberlain et al. 2016). These two TCs have a common denominator: their rapid intensification occurred under preexisting abnormally warm subsurface ocean conditions with high OHC (Foltz and Balaguru 2016; Huang et al. 2017; Rogers et al. 2017). In the case of Hurricane Patricia, OHC reached levels of about 90 kJ cm^{-2}—approximately a factor of 2 larger than the normal conditions in the ENP (Rogers et al. 2017). For Haiyan, the mean OHC was extremely high (above 110 kJ cm^{-2}) during the intensification period (see Table 1). These favorable OHC conditions, along with other favorable conditions such as low vertical wind shear and high sea surface temperatures (SSTs) (Foltz and Balaguru 2016; Huang et al. 2017; Rogers et al. 2017), helped explain the record intensification of the two TCs. However, there are still unresolved questions when comparing these two TCs, for example, in terms of the total time (T_{LMI}) required from the point of genesis to lifetime maximum intensity (LMI), the mean OHC during T_{LMI} (MOHC), and the total accumulated (time-integrated) OHC during T_{LMI} (AOHC) (see appendixes A–C; Wada et al. 2012).

Haiyan reached LMI (87 m s^{-1}) under the condition of high MOHC (117.2 kJ cm^{-2}) and AOHC (1.8 MJ cm^{-2}) in 84 h, while Patricia reached an even higher LMI (95 m s^{-1}), 1.4 times faster (in 60 h), despite having 29% less MOHC (90.7 kJ cm^{-2}) and 55% less AOHC (1.0 MJ cm^{-2}) than Haiyan (Fig. 1; Table 1). In addition to these differences, Patricia's translation speed (4.2 m s^{-1}) was about twice as slow as that of Haiyan (10.1 m s^{-1}) at the LMI stage (Table 1). This makes Patricia's extraordinary intensification even more difficult to explain since our expectation would be that its slower motion should have increased sea surface cooling and hindered heat

Table 1. Comparison of characteristics between Hurricane Patricia and Typhoon Haiyan. Values show the lifetime maximum intensity (LMI; m s^{-1}), accumulated ocean heat content (AOHC; MJ cm^{-2}), three intensification efficiencies (IEs) based on AOHC [m s^{-1} (MJ cm^{-2})$^{-1}$], accumulated sea surface heat content [$ASSHC_{during}$; m s^{-1} (MJ cm^{-2})$^{-1}$], and accumulated air–sea enthalpy flux underneath the TC ($AFLUX_{during}$; m s^{-1} (kW cm^{-2})$^{-1}$], LMI-reaching time (T_{LMI}; h), time required for TC intensification [T_{req}; definition is T_{LMI}/(LMI − 17) × 10; h (10 m s^{-1})$^{-1}$ intensity change in maximum wind speed], average radius at which the wind speed is equal to 64 kt (R64), storm translation speed (V_{storm}; m s^{-1}), vertical wind shear (VWS; m s^{-1}), sea surface temperature before the arrival of the TC (SST_{pre}, °C), sea surface temperature underneath the TC (SST_{during}; °C), cooling effect (SST_{pre} – SST_{during}; °C), ocean heat content (OHC; kJ cm^{-2}) for Hurricane Patricia and Typhoon Haiyan (see appendixes B, C, F). Here, values for R64, V_{storm}, VWS, SST, and OHC represent the means and standard deviations at all track points from the time of genesis to LMI. The three parenthetical values for R64 represent the mean radii (R_{init}, R_{LMI}) when TCs initially achieve the wind speed of 64 kt, or arrive at the LMI stage, and the increasing rate (in percentages, $r_{\Delta R}$) of size from the time of genesis to the LMI stage, respectively. The parenthetical values for V_{storm}, VWS, SST_{pre}, SST_{during}, cooling effect, and OHC represent those at LMI stages. For LMI, AOHC, and IEs, the parenthetical percentages in the "Difference" row are the ratio of the absolute difference (Haiyan – Patricia) to the smaller value. Asterisks denote statistically significant separation in the differences (* = 95% confidence; ** = 99% confidence).

			IE											
	LMI	AOHC	AOHC	$ASSHC_{during}$	$AFLUX_{during}$	T_{LMI}	T_{req}	R64 (R_{init}, R_{LMI}, $r_{\Delta R}$)	V_{storm}	VWS	SST_{pre}	SST_{during}	Cooling effect	OHC
Haiyan	87	1.8	39.6	367.3	1.9	84	12.0	61 ± 15 (28, 76, 171%)	8.3 ± 0.9 (10.1)	6.6 ± 1.1 (5.5)	30.2 ± 0.2 (30.4)	29.8 ± 0.1 (29.6)	0.4 (0.8)	117.2 ± 20.1 (102.7)
Patricia	95	1.0	78.3	561.8	4.1	60	7.6	38 ± 3 (35, 43, 23%)	6.2 ± 1.2 (4.2)	6.9 ± 0.6 (9.3)	29.9 ± 0.1 (29.9)	29.5 ± 0.6 (28.5)	0.4 (1.4)	90.7 ± 14.4 (86.7)
Difference (percentage)	8 (9.2%)	0.8 (80%)	38.7 (98%)	194.5 (53%)	2.2 (116%)	24 (40%)	5.6 (74%)	23 (61%)	2.1** (5.9**)	0.3** (3.8**)	0.3** (0.5**)	0.3** (1.1**)	0.0 (0.6**)	26.5** (16.0%)

energy transfer from the ocean to the TC (Lin et al. 2009). It also should be noted that none of the available forecast guidance, including the most sophisticated, higher-resolution, fully coupled operational models or the best-performing statistical/dynamical models, predicted Patricia's extreme intensification (Kimberlain et al. 2016; Rogers et al. 2017). For Patricia, the most aggressive of the numerical guidance in terms of intensification rate forecasted less than half of the observed rate of intensification (Rogers et al. 2017).

TC intensity prediction is challenging because of the number and complexity of important environmental and dynamical factors, including inner core dynamics and underlying surface forcing, all of which can affect intensity, and yet these factors are not completely understood (Elsberry et al. 2013; Emanuel 1991). In particular, the example of Patricia reinforces that the present understanding of TC intensification mechanisms is limited and that operational TC prediction systems still likely have missing or poorly modeled physical processes affecting intensity. In this study, we aim to address two fundamental questions arising from a comparison of Patricia and Haiyan: 1) What possible characteristics associated with the ENP basin could have contributed to Hurricanes Patricia's unprecedented rapid intensification, despite moving over waters with significantly lower OHC than Haiyan? 2) Did differences in intensification rate between these two TCs originate from geographically specific interbasin characteristics?

A few studies have explored the causes of Patricia's and Haiyan's rapid intensification (Huang et al. 2017; Rogers et al. 2017; Wada et al. 2018), but these studies focused only on the characteristic of those two individual events. Here, we address these questions from a broader interbasin perspective, exploring the climatological behavior of TCs for the ENP and WNP—to which Patricia and Haiyan, respectively, belong—through a combination of reanalysis data and idealized numerical experiments. Particularly, we examine interbasin differences using the time required for TC intensification [T_{req}; h (10 m s^{-1})$^{-1}$], which is defined as the average time required for a TC to increase its intensity by 10 m s^{-1} from genesis, and intensification efficiency (IE), which is defined as intensity change (ΔV) achieved for given oceanic conditions (i.e., per unit of total OHC, sea surface heat content, and air–sea enthalpy flux, accumulated during T_{LMI}) (see appendixes B and C)—the smaller the T_{req} and the greater IE, the faster the

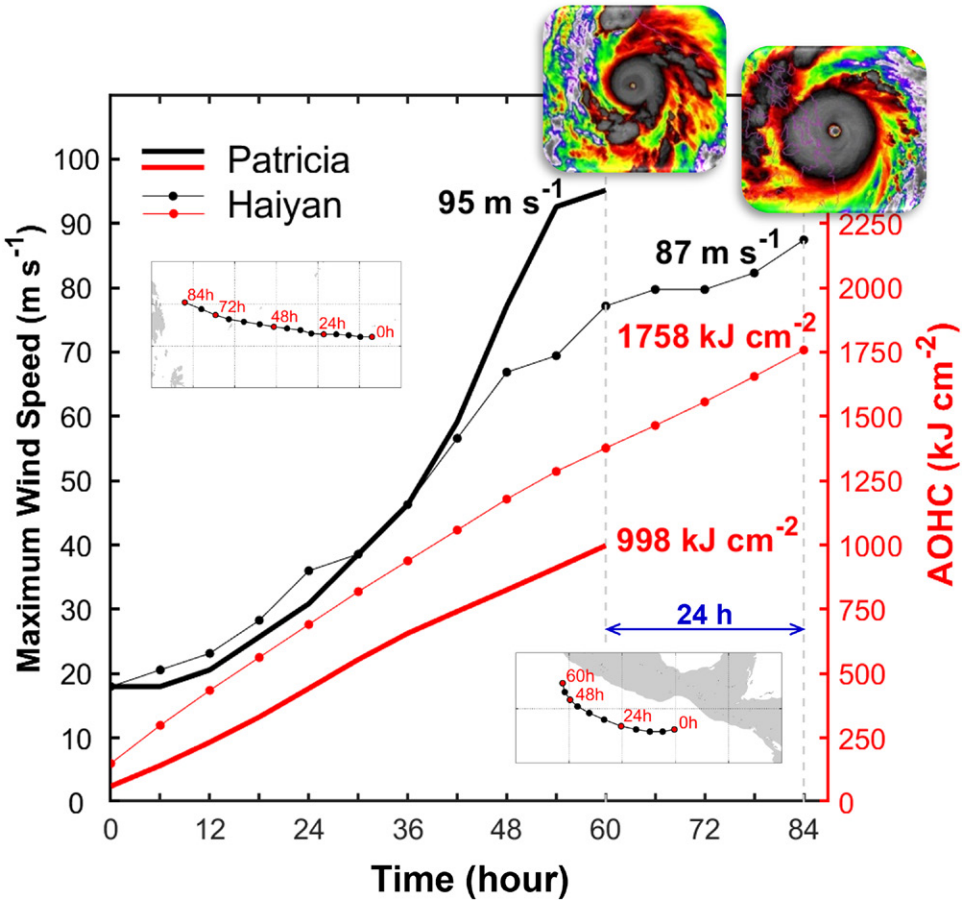

Fig. 1. Comparison of intensity and accumulated ocean heat content (AOHC) between Hurricane Patricia and Typhoon Haiyan. The maximum wind speed (black) and AOHC (red) of the two TCs were compared from time of genesis to time of lifetime maximum intensity (LMI). Pictures represent the NOAA infrared satellite imagery at LMI. The tracks of Haiyan and Patricia are shown in the upper-left and lower-right corners, respectively. The genesis times for Haiyan and Patricia are at 0000 UTC 4 Nov 2013, and 0000 UTC 21 Oct 2015, respectively.

TC reaches a higher LMI in a given oceanic condition. Note that the IE used in this study is a concept similar to fuel efficiency that measures the distance a car can travel using a specific amount of fuel. We hypothesize that analyzing the interbasin characteristics in T_{req} and IE will contribute to a better understanding of TC intensification mechanisms, especially in terms of TC–ocean interactions, and provide some clues for advancing TC intensity prediction skill, which has been slow to advance.

Results

Interbasin difference in TC intensification. First, we calculated T_{req} and IE for 500 TCs occurring in the ENP and WNP from 2001 to 2015 (Fig. 2a). The results reveal that ENP hurricanes require 15% less time to achieve a given intensity increment than WNP typhoons (see T_{req} in Table 2 and Fig. 3a). This is related to the fact that rapid intensification is more common in the ENP than in other basins (Kaplan et al. 2010). Considering that the ENP hurricanes have on average half the available OHC compared to WNP typhoons (see OHC in Table 2 and Fig. 2b), the observed faster intensification in the ENP than in the WNP contradicts our intuition. The AOHC-based IE for ENP hurricanes (89 ± 6 m s^{-1} MJ^{-1} cm^2) is also 2.2 times higher on average than for WNP typhoons (41 ± 2 m s^{-1} MJ^{-1} cm^2) (Table 2 and Fig. 3b). This result implies that ENP hurricanes can reach a given LMI with only 46% of the AOHC needed by WNP typhoons. Interestingly, the IEs of Patricia (78.3 m s^{-1} MJ^{-1} cm^2) and Haiyan (39.6 m s^{-1} MJ^{-1} cm^2) are very similar to the basin mean regression values

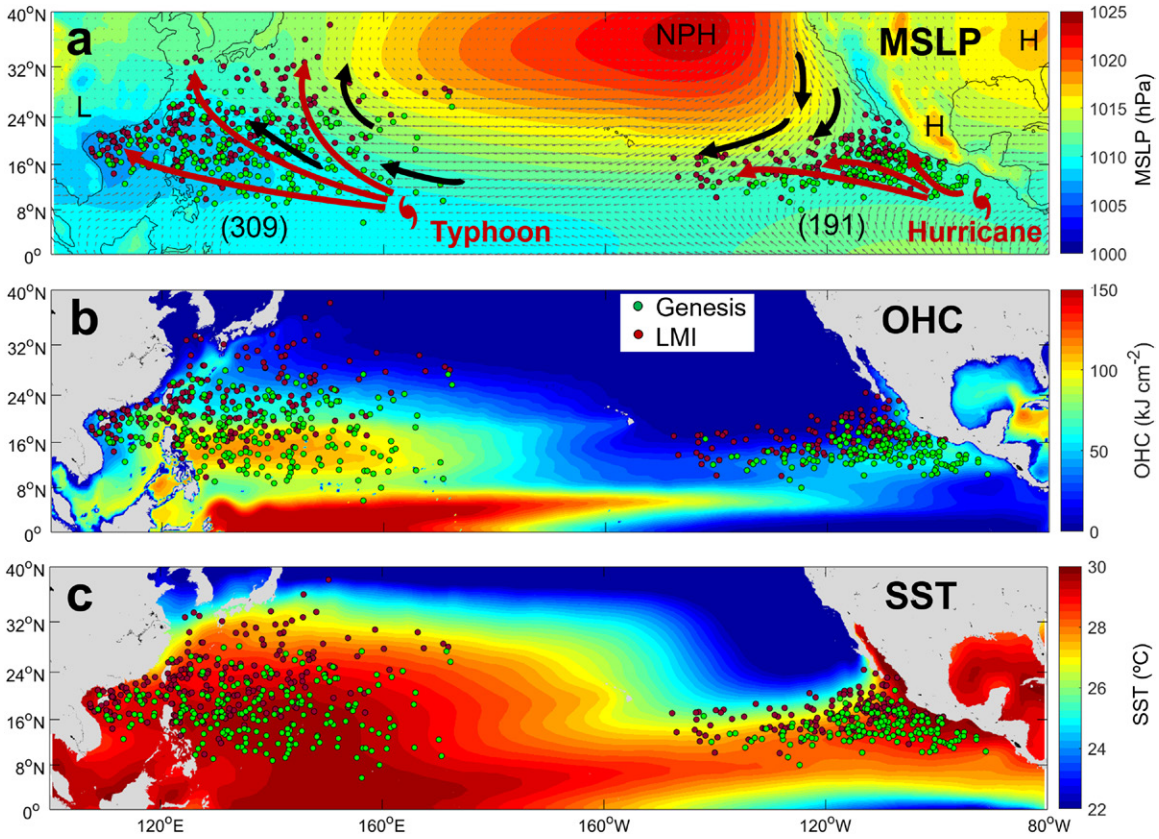

Fig. 2. Comparison of climatological environments between the eastern North Pacific and the western North Pacific. (a) Mean sea level pressure (MSLP; color) and surface wind vectors (small gray arrows) along with schematics showing steering flows (thick black arrows) and typical track patterns (thick red arrows) of Pacific typhoons and hurricanes. H, L, and NPH represent the high and low pressure systems, and the North Pacific high, respectively. (b),(c) Spatial distributions of OHC and SST, respectively. Green and dark purple dots represent the locations at genesis and LMI, respectively, for all TCs that occurred over the peak TC season (July–October), 2001–15. All environmental variables were also averaged over the peak TC season. In (a), parenthetical values indicate the number of TCs used in the analysis.

(see the two filled circles in Fig. 3b and Table 1). This suggests that the significant difference in the AOHC-based IE between these two record-breaking TCs is related to their basinwide characteristics.

Although OHC is widely used in operational TC forecasting (DeMaria et al. 2005), OHC is not a substance that is transferred from the ocean into the atmosphere by contact. In fact, a TC's energy source comes from a thermal disequilibrium (temperature and humidity difference) between the sea surface and the lower atmosphere—all else equal, the larger this disequilibrium, the larger the heat flux (Price 2009). Therefore, the SST underneath a TC (hereafter, SST_{during}), which includes any TC-induced sea surface cooling effect (appendix D), and the resultant sea surface heat content ($SSHC_{during}$) and air–sea enthalpy fluxes ($FLUX_{during}$; appendix C) based on the SST_{during} are the most relevant oceanic properties for TC intensification (Price 2009). In terms of the IEs based on the accumulated $SSHC_{during}$ and $FLUX_{during}$ during T_{LMI} (hereafter, $ASSHC_{during}$ and $AFLUX_{during}$, respectively), we also found that ENP hurricanes intensify more efficiently (by 16%) than WNP typhoons (Table 2 and Figs. 3c,d).

These results have important implications in two respects. First, the relatively small interbasin difference (16%) in the $ASSHC_{during}$-based IE compared to that (117%) in the AOHC-based IE (Table 2) implies that the potential for TC-induced sea surface cooling in the ENP is not fully realized despite lower OHC conditions than in the WNP. Also, only a small fraction (~14%) of the available OHC is used as energy for TC intensification in the WNP (cf. the heat

Table 2. Characteristics related to TC intensification and the background oceanic environments in the eastern/western North Pacific. LMI represents the average lifetime maximum intensity (m s^{-1}); T_{req} represents the average time required for a TC to increase its intensity by 10 m s^{-1} from genesis [h (10 m s^{-1})$^{-1}$]. Three intensification efficiencies (IEs) are calculated based on AOHC [m s^{-1} (MJ cm^{-2})$^{-1}$], accumulated sea surface heat content [$ASSHC_{during}$; unit = m s^{-1} (MJ cm^{-2})$^{-1}$], and accumulated air–sea enthalpy flux underneath the TC [$AFLUX_{during}$; unit = m s^{-1} (kW cm^{-2})$^{-1}$], respectively (see appendixes B and C). Other values indicate ocean heat content (OHC; kJ cm^{-2}), SST before the arrival of the TC (SST_{pre}, °C), mixed ocean temperature to 100-m depth (T_{100}; °C), SST underneath the TC (SST_{during}; °C), cooling effect (SST_{pre} – SST_{during}; °C), potential intensity based on SST_{pre}, SST_{during}, and T_{100} (PI_{SST}, PI_{during}, and PI_{T100}, respectively; m s^{-1}), maximum oceanic Brunt–Väisälä frequency (N^2; $10^{-4} \times s^{-2}$), and relative SST, which is local SST relative to tropical mean SST (R_{SST}; °C), averaged from the time of genesis to the lifetime maximum intensity (LMI) stage for all TCs that occurred in the ENP or WNP from 2001 to 2015. The parenthetical values for OHC, SST, cooling effect, PI, N^2, and R_{SST} represent those at LMI stages. For T_{req} and IE, the parenthetical percentages in the "Difference" row are the ratio of the absolute difference (WNP – ENP) to the smaller value. Asterisks denote statistically significant separation in the differences (* = 95% confidence; ** = 99% confidence).

			IE												
	LMI	T_{req}	AOHC	$ASSHC_{during}$	$AFLUX_{during}$	OHC	SST_{pre}	SST_{during}	Cooling effect	T_{100}	PI_{pre}	PI_{during}	PI_{T100}	N^2	R_{SST}
WNP typhoons	47.9	19.4	41 ± 2	283 ± 14	4.5 ± 0.2	67.7 (51.0)	29.5 (29.5)	28.9 (28.6)	0.6 (0.9)	27.3 (27.3)	76.6 (75.8)	71.2 (67.0)	54.1 (53.3)	4.71 (5.18)	3.0 (2.6)
ENP hurricanes	40.7	16.9	89 ± 6	327 ± 24	5.2 ± 0.5	35.0 (24.2)	28.7 (28.5)	27.8 (27.0)	0.9 (1.5)	24.2 (24.1)	71.9 (70.1)	62.5 (53.8)	18.9 (17.6)	6.08 (5.71)	2.5 (1.9)
Difference (percentage)	7.2** (15%)	2.5** (13%)	48** (117%)	44** (16%)	0.7** (16%)	32.7** (26.8**)	0.8** (1.0**)	1.1** (1.6**)	0.3** (0.6**)	3.1** (3.3**)	4.7** (5.7**)	8.7** (13.2**)	35.2** (35.7**)	1.37** (0.53**)	0.5** (0.7**)

content values at the same LMI in Figs. 3b,c) (Cione and Uhlhorn 2003). Second, the fact that $AFLUX_{during}$-based IE is higher in the ENP than in the WNP means that, for a given amount of ocean energy, ENP hurricanes can intensify to higher LMI than WNP typhoons. Some of the reasons for these findings, focusing on the atmosphere, can be inferred from previous studies (Xu et al. 2019), but here we present new additional factors that contribute to this behavior such as TC size, TC latitude, vertical wind shear, ocean waves, and air–sea temperature/humidity differences. Particularly, we address why TC-induced sea surface cooling is only slightly larger in the ENP than the WNP, despite the much greater potential for cooling in the ENP. Toward this end, the following analysis compares the climatological characteristics of the ENP and WNP for various indices known to affect TC-induced sea surface cooling and TC intensification.

Relationship between TC size and intensity. A pronounced interbasin difference between ENP and WNP TCs is their size, defined as the average radius of 34-, 50-, and 64-kt (1 kt ≈ 0.51 m s^{-1}) winds (hereafter, R34, R50, and R64, respectively); WNP typhoons are, on average, 23%–44% larger than ENP hurricanes (Table 3). An idealized numerical experiment (Kilroy and Smith 2017) showed that the smaller the TC size, the faster the intensification, because deep convection is focused closer to the vortex axis, resulting in a faster spinup for smaller TCs. Smaller TCs tend to have a greater pressure gradient near the eyewall than large TCs (Hoarau et al. 2017) because the pressure gradient is distributed over a smaller radial distance, leading to stronger maximum wind speed for a given central minimum pressure (Knaff and Zehr 2007). A statistical analysis (Carrasco et al. 2014) also showed that TCs undergoing rapid intensification are often significantly smaller than those that do not, and TC size (particularly, R34) has a strong negative correlation with the change in intensity. It is also known that the larger the TC size (i.e., R34, R50, and R64), the stronger the sea surface cooling, mainly due to the longer duration of intense TC winds for a given point in the ocean (Price 1981; Pun et al. 2018; Lin et al. 2021).

An idealized numerical experiment for a category-4 TC (wind speeds of 113–136 kt on the Saffir–Simpson scale) under oceanic conditions for the ENP (Fig. 4; appendix E) reveals that, for a constant forward speed, a relatively smaller TC (like an ENP hurricane) produces a maximum sea surface cooling of 6°C, while a relatively larger TC (like a WNP typhoon)

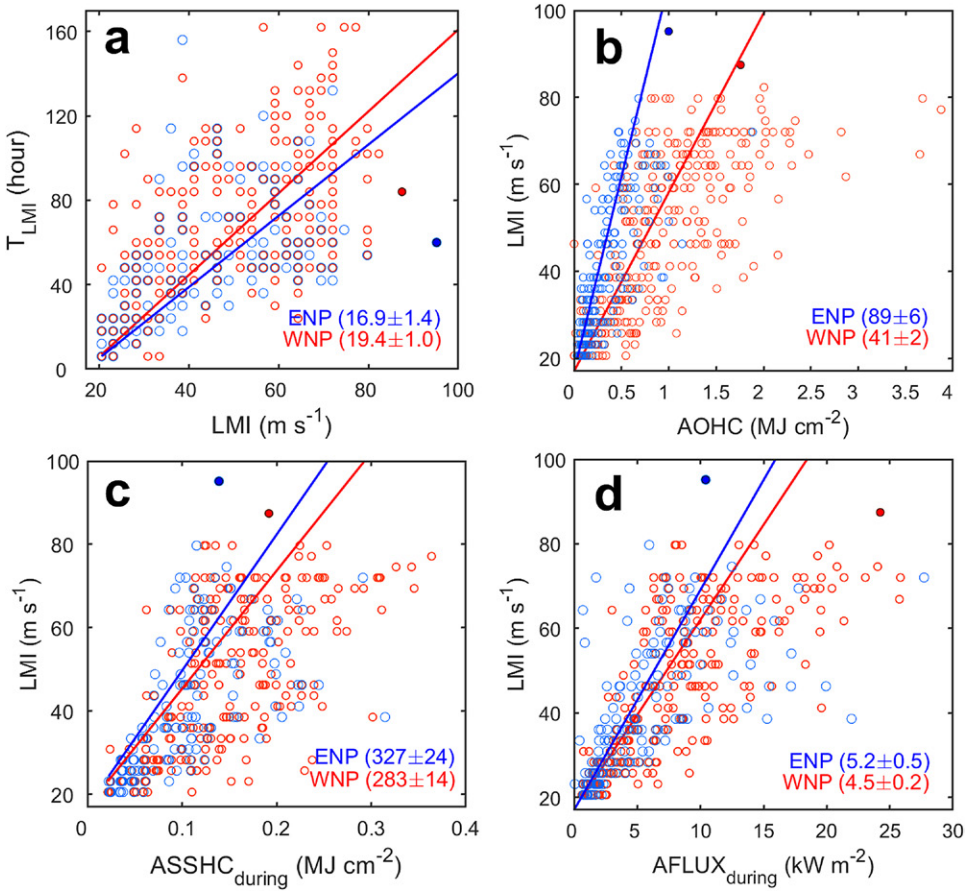

Fig. 3. Comparison of the time required for TC intensification (T_{req}) and three intensification efficiencies (IEs) for TCs that occurred in the ENP and WNP from 2001 to 2015. (a) Scatterplot of the LMI-reaching time (T_{LMI}) from genesis against LMI. (b)–(d) Scatterplots of LMI against accumulated ocean heat content (AOHC), sea surface heat content ($ASSHC_{during}$), and air–sea enthalpy fluxes ($AFLUX_{during}$), in which "during" represents using SST underneath a TC (SST_{during}) (see appendixes B–D). The slopes of regression functions (solid lines) are a measure of T_{req} and IEs, respectively. The mean values of T_{req} and IEs for each basin and 95% two-sided confidence bounds are shown. The blue and red filled circles for the ENP and WNP denote the values for Hurricane Patricia and Typhon Haiyan, respectively.

produces cooling up to 8°C (Figs. 5a,b), which is consistent with previous results (Price 1981; Lin et al. 2021). The ~2°C reduction in cooling for the (smaller) ENP hurricanes implies a crucial role for TC size in limiting to some extent the potentially large TC-induced surface cooling for ENP hurricanes that is potentially large due to factors such as the basin's shallow mixed layer and steep thermocline.

The significant difference in average TC size between the ENP and WNP develops mostly during the intensification period. For example, the mean R34 values for ENP hurricanes and WNP typhoons when the storms first reach 34-kt wind speeds (R_{init}), were 92 and 100 km (only 9% difference), respectively; however, at LMI, this difference has increased to 42% (143 and 204 km, respectively) (Table 3). This implies that WNP typhoons increase in size about twice as much as ENP hurricanes do during their intensification phase (104% versus 55%, respectively). For R50 and R64, the difference in the increasing rate ($r_{\Delta R}$) for the two basins is even greater, reaching up to 2.2 times (Table 3). Surprisingly, Haiyan's size increased 7.4 times more than Patricia's during the intensification period ($r_{\Delta R}$ was 171% and 23% for Haiyan and Patricia, respectively; Table 1). This may be related to the fact that the difference (116%; Table 1) in $AFLUX_{during}$-based IE between the two TCs is much larger than that in the basin average (16%; Table 2). All these results indicate that the large increase in TC size during intensification appears to be one of the major factors leading to the relatively slow intensification of Haiyan

Table 3. Comparison of characteristics between eastern North Pacific (ENP) hurricanes and western North Pacific (WNP) typhoons and their background atmospheric environments. Values show TC size (R34, R50, R64; km), latitude of TC center (LAT; °N), storm translation speed (V_{storm}; m s^{-1}), the residence time (RT; h), vertical wind shear (VWS; m s^{-1}), inertial stability (IS; $10^{-4} \times s^{-2}$), convective available potential energy (CAPE; J kg^{-1}), static stability (SS; $10^{-6} \times s^{-2}$), moist static energy (MSE; $10^3 \times$ kJ kg^{-1}), relative humidity (RH, %), the sea–air difference in specific humidity ($q_s - q_a$; g kg^{-1}) and temperature (SST – T_a; °C) at the air–sea interface, averaged from the time of genesis to the lifetime maximum intensity (LMI) stage for all TCs that occurred in the ENP or WNP from 2001 to 2015. The parenthetical values for all metrics except TC size represent those at LMI stages. The first three parenthetical values for R34, R50, and R64 (denoted in the WNP and ENP) represent the mean radii (R_{init}, R_{LMI}) when TCs initially achieve (R_{init}) the wind speeds of each radius (i.e., 34, 50, and 64 kt) or arrive at the LMI stage (R_{LMI}), and the increasing rate (in percentages, $r_{\Delta R}$) of size from the time of genesis to the LMI stage, respectively. The last parenthetical values for R34, R50, and R64 (denoted in the WNP) represent the ratio of $r_{\Delta R}$ between the two basins. For R34, R50, and R64, the parenthetical percentages in the "Difference" row are the ratio of the absolute difference (WNP – ENP) to the smaller value. Asterisks denote statistically significant separation in the differences (* = 95% confidence; ** = 99% confidence).

	R34 (R_{init}, R_{LMI}, $r_{\Delta R}$)	R50 (R_{init}, R_{LMI}, $r_{\Delta R}$)	R64 (R_{init}, R_{LMI}, $r_{\Delta R}$)	LAT	V_{storm}	RT	VWS	IS	CAPE	SS	MSE	RH	$q_s - q_a$	SST – T_a
Typhoons in the WNP	156 (100*, 204**,104, 1.9%)	75 (46, 102**, 120, 2.2%)	52 (37**, 65**, 77, 2.2%)	17.7 (20.5)	5.0 (5.5)	14.3 (15.8)	7.7 (8.3)	8.7 (10.0)	652.7 (765.7)	177.9 (181.3)	338.6 (338.0)	63.5 (69.0)	1.10 (0.94)	11.28 (10.83)
Hurricanes in the ENP	119 (92/143/55%)	61 (46/74/54%)	36 (31/42/36%)	15.2 (16.6)	4.6 (4.5)	11.3 (12.1)	6.0 (6.1)	7.7 (8.8)	328.6 (538.2)	178.1 (181.6)	336.9 (336.1)	61.3 (65.4)	1.48 (1.31)	11.37 (10.88)
Difference (percentage)	37** (31%)	14** (23%)	16** (44%)	2.5** (3.9**)	0.4** (1.0**)	3.0* (3.7**)	1.7** (2.2**)	1.0** (1.2**)	324.1** (227.4**)	−0.2 (−0.3)	1.7** (1.9**)	2.2** (3.6**)	−0.38** (−0.37**)	−0.09 (−0.05)

and WNP typhoons in general; conversely, they partly explain how smaller ENP hurricanes like Patricia can overcome lower OHC conditions and intensify more rapidly.

Roles of ocean waves. When the influence of TC-induced ocean waves is considered, the difference in TC size between the two basins plays an even more significant role in the TC intensification process. An idealized numerical experiment (see appendix E) reveals that a large category-4 typhoon produces a higher significant wave height and longer mean wavelength in its TC core region, where the strongest winds and sea surface cooling occur, compared to a smaller hurricane with the same intensity (Fig. 5c; Figs. 6a–f). In these experiments, the maximum differences were 40 and 3 m for wavelength and significant wave height, respectively. These differences are mainly the result of increased fetch and duration associated with increased TC size (Moon et al. 2004; Young 2017). Such changes in wave characteristics can influence TC intensification through at least two physical processes: sea spray and wave-induced mixing.

First, the increase in wavelength and significant wave height, as for a large WNP typhoon, leads to an increase in the phase speed and a decrease in wave steepness (due to the greater increase in wavelength than in significant wave height) (Figs. 6g–l). This provides a condition unfavorable for sea spray generation, because of the reduction of both wind forcing and wave breaking (Xu et al. 2021a). Thus, it has negative feedback on intensification for a larger TC since an increase in sea spray is known to increase the sea–air enthalpy transfer (Andreas and Emanuel 2001; Bao et al. 2011; Wang et al. 2001; Xu et al. 2021b). Second, increased significant wave height and wavelength enhances the TC-induced sea surface cooling (Figs. 5a,b) due to the additional wave-induced mixing from unbroken surface waves, which induce both under-TC cooling and ahead-of-TC cooling due to waves propagating faster than the storm (Aijaz et al. 2017; Babanin 2006; Stoney et al. 2017; Walsh et al. 2017). Both of these wave-related processes lead to less favorable conditions for the intensification of a large WNP typhoon, providing an additional explanation for why large typhoons statistically have relatively low IE.

Background oceanic environments. In the ENP, on average, the available OHC along TC tracks is about 1.9 times lower than the WNP (Table 2); the mixed layer depth is also much shallower

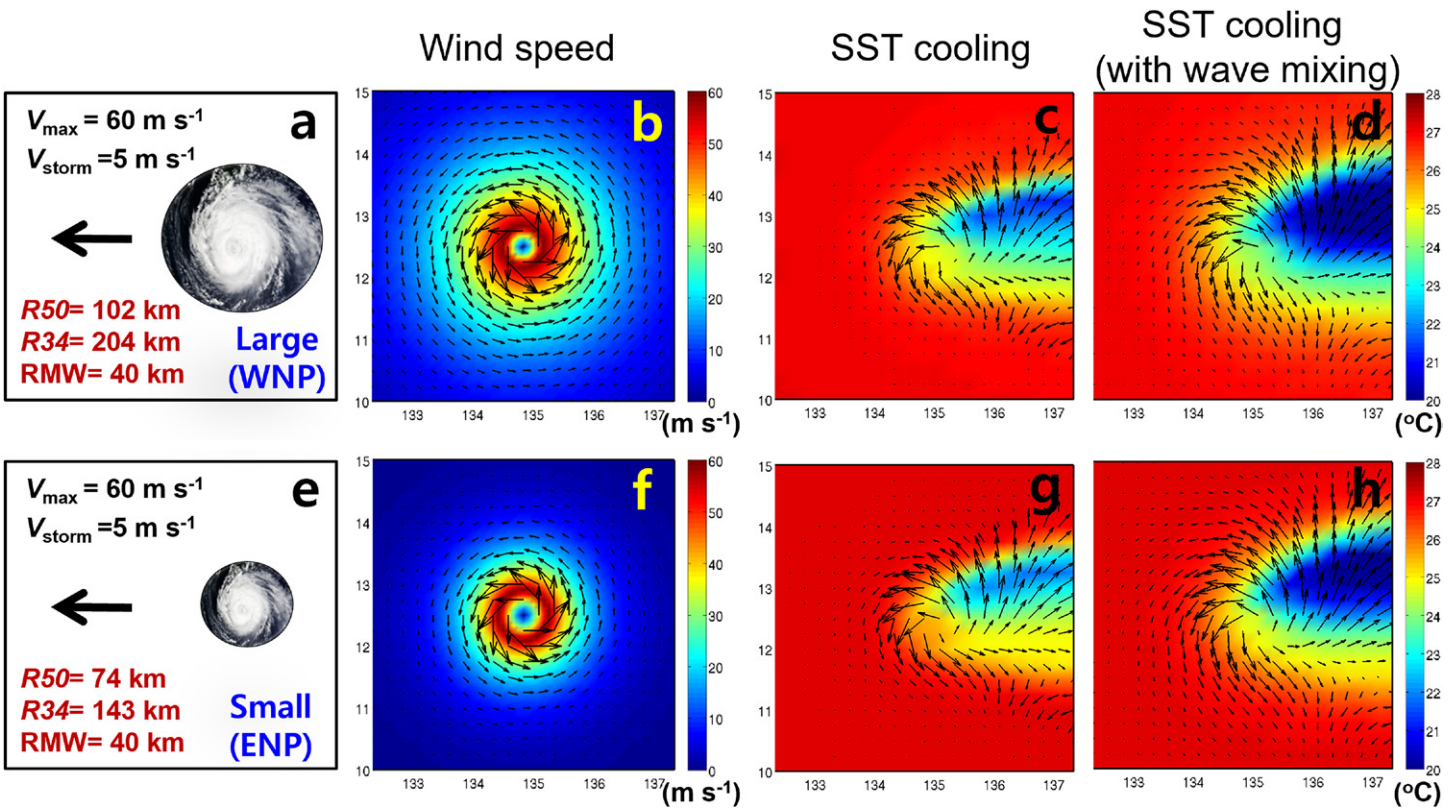

Fig. 4. Comparison of TC-induced sea surface cooling between the WNP and the ENP. (a),(e) Two idealized moving-TC experiments investigating the effect of TC size on sea surface cooling, using the mean radii of 34-kt (R34) and 50-kt (R50) winds, and the radius of maximum wind (RMW) obtained from the WNP and the ENP observations at LMI stages, with maximum wind speed (V_{max}) and storm translation speed (V_{storm}) specified as 60 and 5 m s^{-1}, respectively. (b),(f) The spatial distributions of wind speeds and vectors; surface ocean current vectors and SST variations (c),(g) without and (d),(h) with wave-induced mixing in the WNP and the ENP were obtained after 54 h, when a steady-state condition was achieved (see appendix E).

and the slope of the thermocline (or pycnocline) is steeper in the ENP than in the WNP (Figs. 7a,b). This suggests that the potential for TC-induced sea surface cooling is much greater in the ENP than in the WNP (Lin et al. 2008). In fact, under these conditions, if a TC mixes water to the 100-m depth, regarded as a typical mixing depth by intense TCs (Price 2009), the resulting depth-averaged temperature (T_{100}) is 3.1°C lower in the ENP than in the WNP (Table 2).

In the ENP, the preexisting SST (SST_{pre}) before the arrival of the TC is 0.8°C lower than that in the WNP; the preexisting average uncoupled potential intensity (PI_{pre}; Emanuel 1999) is only slightly (4.7 m s^{-1}) smaller in the ENP (Table 2). However, considering the vertical mixing to the same depth in both basins produces a significant difference in the coupled potential intensity (PI_{T100}) (Lin et al. 2013) (appendix C), wherein the value for ENP hurricanes (18.9 m s^{-1}) is only one-third of that for WNP typhoons (54.1 m s^{-1}). This result emphasizes that the fast and efficient intensification of ENP hurricanes cannot occur without a significant reduction in ocean mixing compared to WNP typhoons.

As stated in earlier discussions, ENP hurricanes induce less ocean mixing than WNP typhoons do under the same oceanic conditions due to the former's smaller size. Aside from this factor, a strong stratification in the pycnocline, mainly due to a sharp temperature reduction with depth in the upper ocean, can inhibit vertical mixing in the ENP (Shay and Brewster 2010). A comparison of the maximum Brunt–Väisälä frequency (N^2), known as a stratification parameter (WNP = 4.71 × 10^{-4} s^{-2}, ENP = 6.08 × 10^{-4} s^{-2}; Table 2), reveals that seawater in the ENP makes vertical mixing 1.3 times more difficult than seawater in the WNP under the same wind forcing because a larger Brunt–Väisälä frequency requires proportionally larger wind-forced shears for vertical mixing to occur (Shay and Brewster 2010). Separating

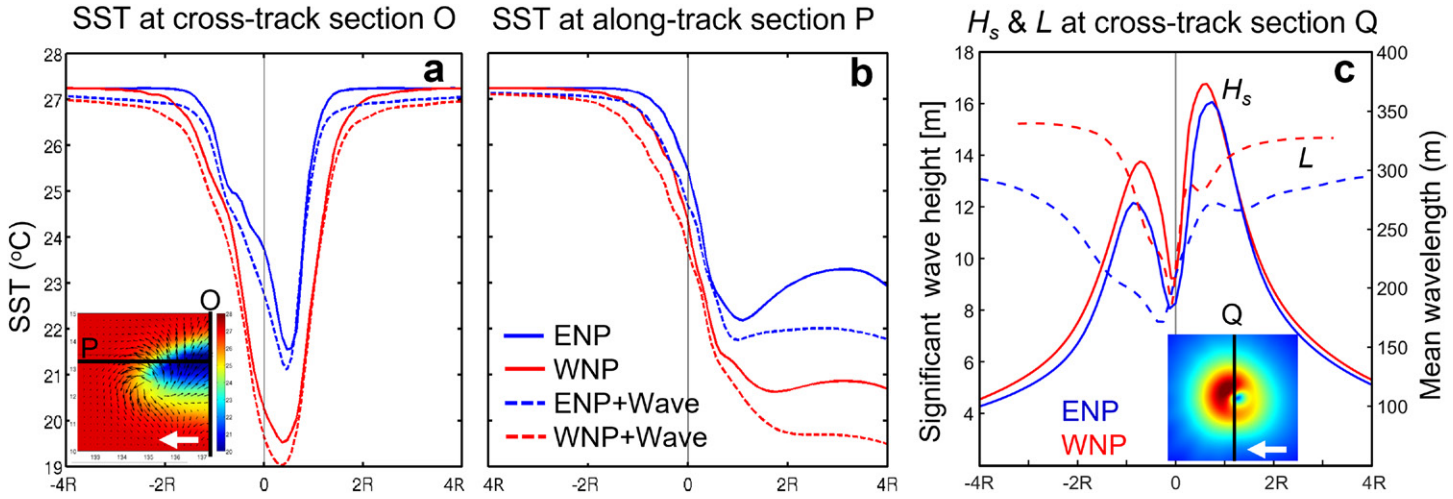

Fig. 5. Impacts of TC size on the sea surface cooling and wave characteristics from ideal moving-TC experiments. (a),(b) Cross- and along-track SST variations; the thick solid lines (P and O) show the locations of sections. "Small" and "Large" mean the experiments using the mean size of hurricanes (ENP) and typhoons (WNP), respectively (see Fig. 4). "Wave" means that wave-induced mixing is additionally considered in the experiment. (c) Significant wave height (H_s, solid lines) and mean wavelength (L, dashed lines) at the cross-track section Q. SST, H_s, and L were obtained after 54 h, when a steady-state condition was achieved, and the x axis was normalized using the mean radius of 50-kt wind (see appendix E). This figure illustrates that a large TC (WNP typhoon) produces more sea surface cooling, higher significant wave height, and longer wavelengths than a small TC (ENP hurricane) having the same intensity and translation speed.

the temperature and salinity contributions to the Brunt–Väisälä frequency reveals that salinity also plays some role in producing the strong density stratification in the ENP, although the large vertical temperature gradient is the key factor (Figs. 7c,d). The strong halocline gradient in the main TC passage region of the ENP originates from the extension of the remarkably fresh surface water west of Colombia and in the Gulf of Panama, originating from the strong precipitation in the region (Johnson et al. 2012) (Fig. 7e).

The analysis reveals that the SST and coupled potential intensity during TC passage, estimated using the actual TC size, translation speed, stratification, and water temperature–salinity profiles in the two basins (see SST_{during} and PI_{during} in Table 2; appendix D), differs by only 1.1°C and 8.7 m s^{-1} in both basins, respectively. This implies that the strong potential for oceanic surface cooling is typically not fully realized in the ENP basin due to the factors aforementioned (which otherwise could potentially provide strong negative feedback on intensity). It also should be noted that the average TC-induced SST cooling in the ENP (0.9°C) is still larger than that in the WNP (0.6°C) due to an inherently lower OHC (see cooling effect in Table 2). Given that larger cooling corresponds to less flux, this reemphasizes that ENP hurricanes intensify more efficiently than WNP typhoons despite adverse ocean conditions.

Background atmospheric environments. A comparison of environmental atmospheric metrics influencing a TC's intensification reveals that some conditions are more favorable to WNP typhoons than to ENP hurricanes because high inertial stability, convective available potential energy, and moist static energy in the WNP (Table 3) are known to help TCs sustain deep Rossby penetration depths and active convection (Foltz et al. 2018; Holland and Merrill 1984; Huang et al. 2017; Merrill 1988; Wada et al. 2012). Higher environmental relative humidity in the WNP may also provide a favorable condition for TC intensification (Wu et al. 2012). However, note that the favorable atmospheric conditions in the WNP also provide conditions conducive for increasing TC size (Chan and Chan 2014; Hill and Lackmann 2009), which can diminish TC intensification efficiency in the WNP.

For vertical wind shear (VWS), a major dynamic index affecting TC intensity (Kaplan and DeMaria 2003; Tao and Zhang 2015), the ENP has 28% lower values (6.0 ± 2.7 m s^{-1}) than

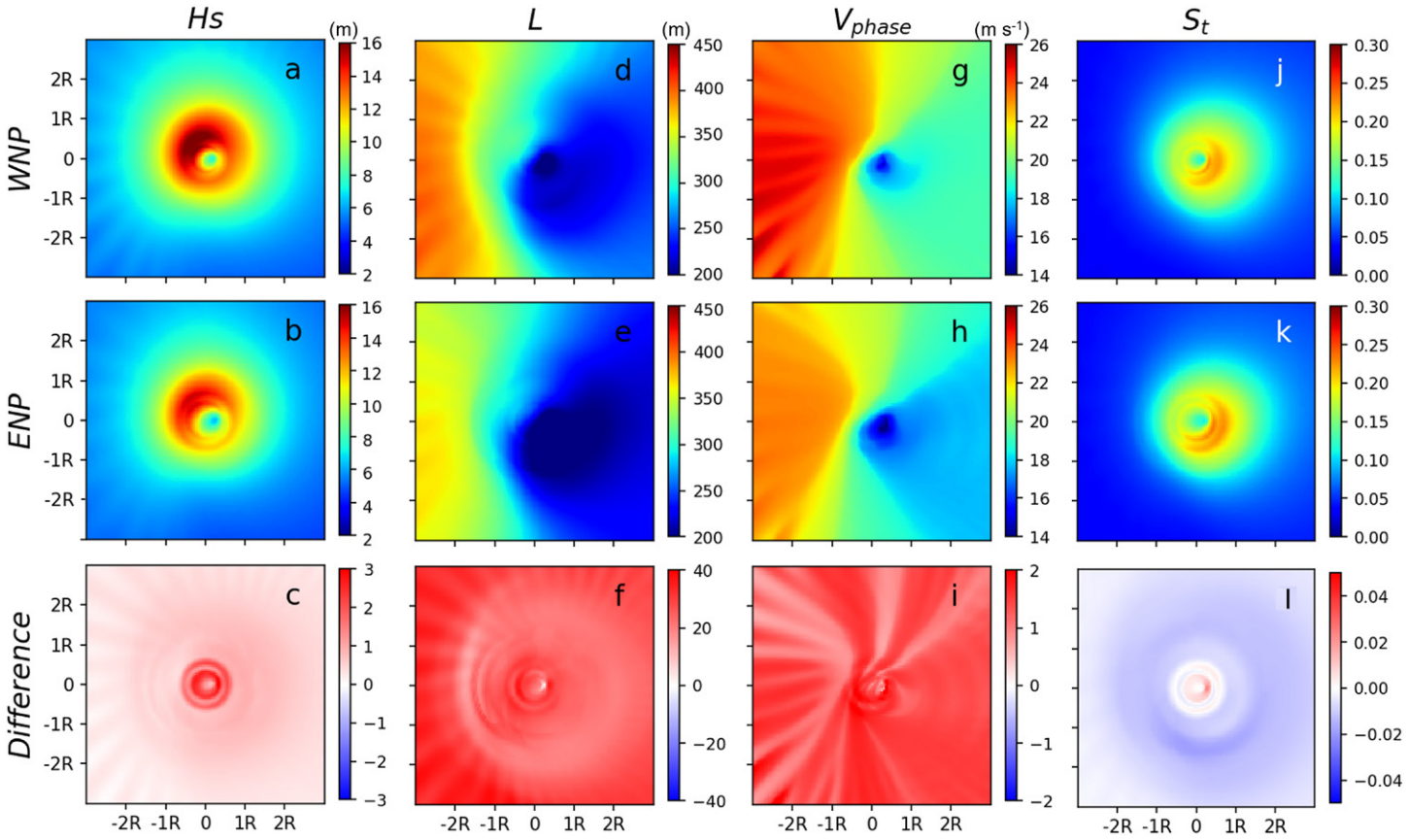

Fig. 6. Comparisons of wave characteristics for steady-moving (5 m s^{-1}) large WNP and small ENP TCs. The spatial distributions of (a),(b) significant wave height (H_s); (d),(e) mean wavelength (L); (g),(h) mean phase speed (V_{phase}); and (j),(k) mean steepness (S_t) in the WNP and ENP, as well as (c),(f),(i),(l) their differences, were obtained after 54 h, when a steady-state condition was achieved (see appendix E). Axes were normalized using R50. This figure illustrates that a large TC (WNP typhoon) produces higher significant wave height, longer wavelength, faster phase speed, and lower wave steepness than a small TC (ENP hurricane) for the same intensity and propagation speed.

the WNP has (7.7 ± 3.0 m s^{-1}) (see VWS in Table 3). For air–sea specific humidity difference at the interface, which helps determine the latent heat flux supplied from the ocean (Huang et al. 2017), the ENP has higher values (1.48 g kg^{-1}) than the WNP has (1.10 g kg^{-1}). Thus, these two factors provide more favorable conditions for the intensification of ENP hurricanes. In particular, given that a VWS difference of only 1.5 m s^{-1} has a large effect on the timing of rapid intensification (Tao and Zhang 2015), the significant interbasin difference (1.7 m s^{-1}) in VWS could contribute substantially to the faster intensification of ENP hurricanes.

The SST underneath a TC, $\mathrm{SST}_{\mathrm{during}}$, is on average higher in the WNP than in the ENP, which contributes to a higher mean $\mathrm{PI}_{\mathrm{during}}$ in the WNP (Table 2). However, a comparison of the $\mathrm{PI}_{\mathrm{during}}$ as a function of $\mathrm{SST}_{\mathrm{during}}$ shows for most SSTs (above 27°C), the $\mathrm{PI}_{\mathrm{during}}$ is greater in the ENP than in the WNP (Fig. 8a). This indicates that the ENP has more favorable atmospheric conditions for TC intensification than the WNP under the same ocean conditions. A component analysis (Wing et al. 2015) shows that this is due to differences in the thermodynamic disequilibrium term ($h_o^* - h^*$) (Figs. 8b,c), probably due to the colder (warmer) troposphere and drier (wetter) boundary layer in the ENP (WNP) (Xu et al. 2019). In the thermodynamic efficiency term $[(T_s - T_o)/T_o]$, the WNP has higher values at SSTs above 27°C due to a lower outflow-layer air temperature (T_o) (Xu et al. 2019), but this term contributed little to the variation of the $\mathrm{PI}_{\mathrm{during}}$ (Fig. 8c).

Role of latitudes. It is known that TCs at low latitudes intensify more rapidly on average than those at higher latitudes. This is due to stronger and deeper friction-induced inflow

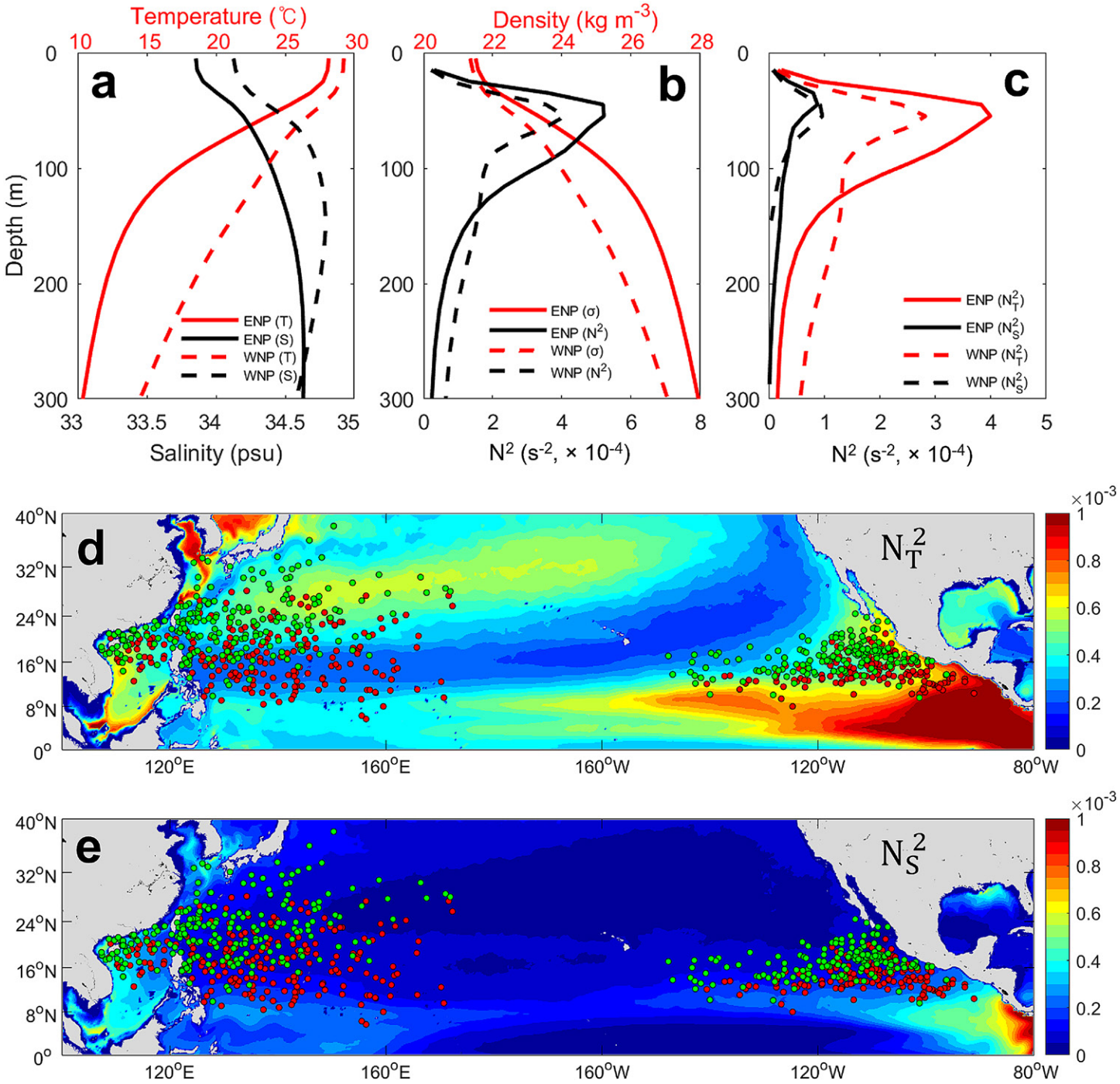

Fig. 7. Comparison of water properties between the ENP and WNP. Vertical profiles of (a) temperature and salinity, (b) density, and (c) Brunt–Väisälä frequency (N^2). (d),(e) Spatial distributions of temperature-derived N^2 (N_T^2) and salinity-derived N^2 (N_S^2), which were averaged over the peak TC season (July–October). All vertical profiles were obtained by averaging the values of all the track points (6-h intervals) from the genesis (red dots) to the LMI (green dots) from July to October 2001–15, in the WNP and the ENP, respectively.

under a lower planetary vorticity (small Coriolis parameter) environment and much larger diabatic heating rate, along with a larger radial gradient of diabatic heating above the boundary layer (Li et al. 2012; Smith et al. 2015). In the ENP, once the TCs move away from the Mexican coast, their tracks mostly have a strong westward component and are confined to a relatively narrow low-latitude region south of 20°N (Fig. 2a). This is due to the typical circulation (northerly to easterly winds; see thick black arrows in Fig. 2a) around the North Pacific high (Wood and Ritchie 2015). In the WNP, tracks are more distributed across a broad region meridionally, even reaching north of 30°N (see thick red arrows in Fig. 2a). Analysis

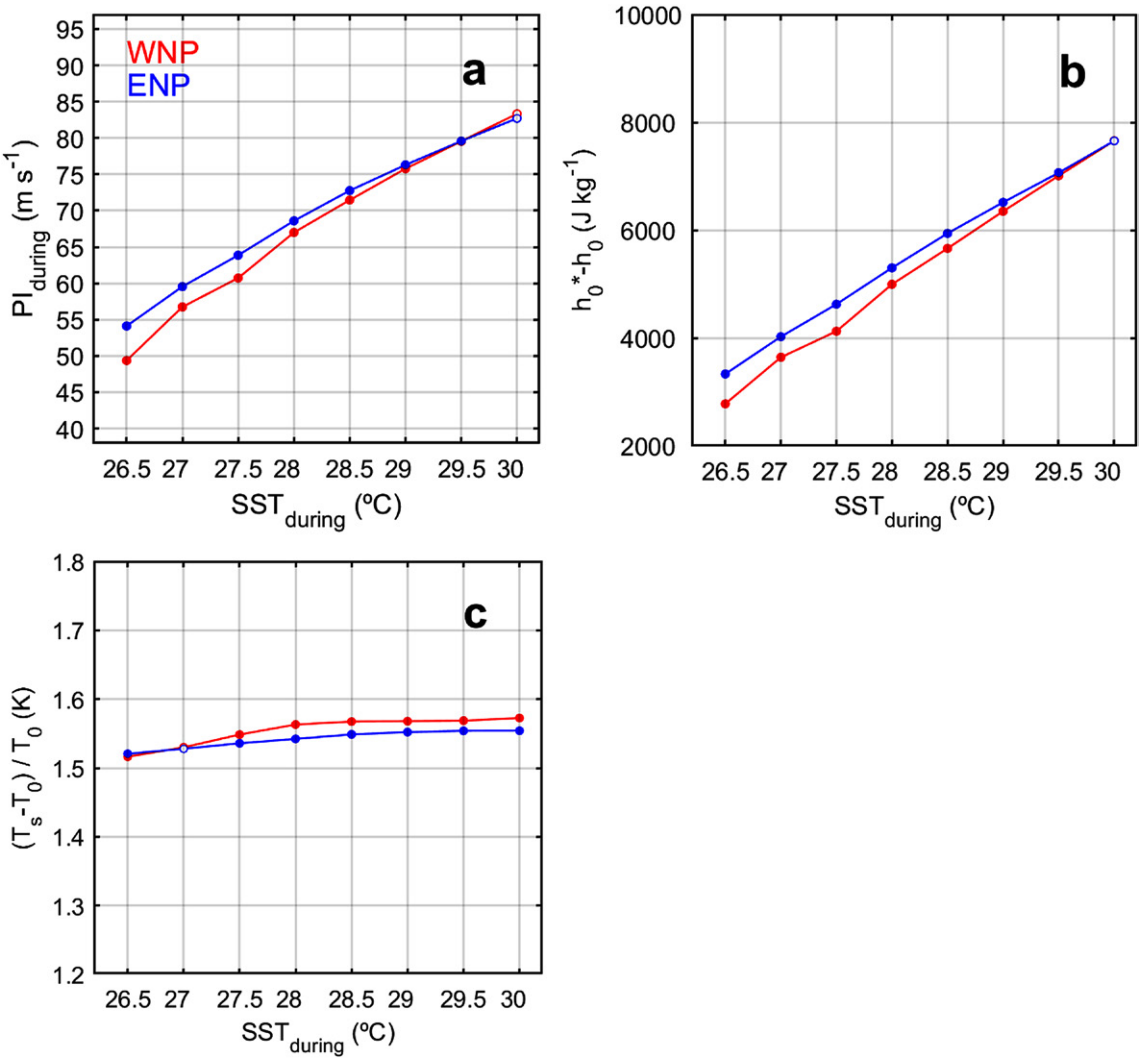

Fig. 8. The averages of (a) TC potential intensity (PI_{during}) and its components [(b) thermodynamic disequilibrium term and (c) thermodynamic efficiency term] against SST underneath a TC (SST_{during}) in the WNP and ENP. In each basin, the means of values are calculated at each 0.5°C bin for SST_{during} between 26.5° and 30°C, based on the approach similar to Xu et al. (2019). Filled circles denote statistically significant separation in the differences at 95% confidence level.

reveals that the difference in the mean TC occurrence latitude between the two basins is 2.5° and reaches up to 3.9° at the LMI stage (Table 3). Latitude is also believed to affect TC size. Observations suggest that the more frequent TC movement to higher latitudes contributes to the increased occurrence of larger TCs there (Chan and Chan 2013). Idealized modeling studies (Chavas and Reed 2019) also support a link between increasing latitude in the tropics and increased TC size. The higher average latitude of TC occurrence in the WNP basin thus may contribute to the larger TC sizes there relative to the ENP and through that mechanism may also contribute to the slower TC intensification in the WNP.

Isolated effect of factors related to TC intensification. A limitation of this study is that it does not provide a quantitative assessment of which factors predominately contribute to the faster development of ENP hurricanes, given that they have less available ocean energy than WNP typhoons. For example, in the case of vertical wind shear and relative humidity, known as the most important atmospheric environments for TC intensification (Merrill 1988; DeMaria and Kaplan 1994; Kaplan and DeMaria 2003; Tao and Zhang 2015; Wu et al. 2012), as well as latitude and TC size (R34), a question arises whether their average differences between the two basins (1.7 m s^{-1}, 2.2%, 2.5°, 37 km,

respectively; Table 3) could play a major role in the IE difference. Another related question is that how the IE difference between the two basins would change if the ENP and WNP TCs were subsetted to only include cases with favorable conditions for TC intensification—vertical wind shear (≤5 m s^{-1}), environmental relative humidity (≥66%), latitude (≤16°N), and TC size (R34; ≤100 km) (see Table 4).

Because the TC intensification process is complex, it is possible that the selected sample is favorable for TC intensification for one condition but not for another. Such complexity makes it difficult to estimate which factor is primarily responsible for the IE differences. However, if a significant IE difference between WNP and ENP in all samples disappears or reverses in a storm subset controlling for a single specific factor, this can at least be considered as a major factor driving the IE differences. Further analysis for the subsets of the four factors defined earlier reveals that the interbasin differences for T_{req} and IEs (particularly, based on $ASSHC_{during}$ and $AFLUX_{during}$) were still statistically significant (or even increased in some cases) for TC subsets with the favorable vertical wind shear, relative humidity, and latitude conditions. However, the interbasin differences were no longer significant (even reversed) under the small TC size condition (Table 4). This suggests that air–sea interaction processes related to TC size play a central role in explaining the interbasin IE differences.

Summary and discussion

The tropical WNP region has the world's largest pool of deep warm waters, enhanced due to easterly trade winds, and thus has some of the highest OHC in the Northern Hemisphere (Fig. 2). The mean WNP environment features high atmospheric convective available potential energy, high relative humidity, high SST, and high potential intensity (Tables 2 and 3), which are extremely favorable for TC development. However, WNP typhoons intensify more slowly on average than ENP hurricanes. We infer that this is mainly because WNP typhoons tend to increase their size significantly, by 77%–120% (Table 3) on average, during their intensification period due to various beneficial conditions for increasing their TC size such as large initial vortex (Kilroy and Smith 2017; Xu and Wang 2010), high relative SST (Chavas et al. 2016; Lin et al. 2015), favorable synoptic flow patterns (Liu and Chan 2002), monsoonal (high moisture) environment (Lovelock 2003; Wang 2012; Xu and Wang 2010), and relatively high average latitude of TC occurrence (Chan and Chan 2013; Chavas and Reed 2019) (see appendix G). Larger TCs lead to longer wind forcing of the ocean, higher wave heights, longer wavelengths, smaller pressure gradients, stronger ocean mixing and sea

Table 4. Differences in various indices related to intensification efficiency between WNP and ENP for all TCs and subsets. Comparisons were made for all TCs and subsets with the same favorable conditions for vertical wind shear (VWS), environmental relative humidity (RH), latitude (LAT), and TC size (radius of 34-kt winds; R34) for both basins. Conditions favorable for TC intensification are defined as the top 20%–22% of each variable in terms of WNP. That is, the time required for TC intensification (T_{req}) and intensification efficiencies (IEs) are obtained for TCs with mean VWS, RH, and R34 from the time of genesis to the LMI of less than 5 m s^{-1}, greater than 66%, and less than 100 km, respectively (including TCs that achieved their LMI south of 16°N). The numbers (percentages) of WNP and ENP TCs subsampled are 61 (20%) and 76 (40%) for VWS, 68 (22%) and 75 (39%) for LAT, 68 (22%) and 33 (170%) for RH, and 61 (20%) and 50 (26%) for R34, respectively. Asterisks denote statistically significant separation in the differences (* = 95% confidence; ** = 99% confidence). Refer to Table 2 for the definition and unit of each index.

		Subsets			
Differences (WNP – ENP)	All TCs	VWS (≤5m s^{-1})	LAT (≤16°N)	RH (≥66%)	R34 (≤100 km)
T_{req}	2.5**	4.7**	3.0**	1.6*	–1.0
AOHC-based IE	–48**	–65**	–42**	–52**	–36**
$ASSHC_{during}$-based IE	–44**	–140**	–70**	–45**	29
$AFLUX_{during}$-based IE	–0.7**	–2.1**	–1.2**	–1.1**	0.4

surface cooling, and less sea-spray generation (Fig. 9). Each of these processes can contribute toward reduced occurrence of extreme rapid intensification of WNP typhoons. Moderation of strong low-level inflow by movement of typhoons to higher latitudes (Smith et al. 2015), relatively higher vertical wind shear, warmer troposphere, and wetter boundary layer are additional factors that can slow their intensification in the WNP.

In comparison, ENP hurricanes encounter several less favorable environmental conditions than WNP typhoons, including slightly lower SST, OHC, and PI underneath a TC (Table 2), and greater potential for storm-induced ocean surface cooling due to a shallower warm upper-ocean layer. However, the large potential SST cooling in the ENP is at least partially countered by increased upper-ocean density stratification (Shay and Brewster 2010), smaller average TC size, and related wave-interaction effects, which reduce vertical mixing and result in only slightly larger SST cooling for TCs in the ENP than WNP. Meanwhile, relatively lower vertical wind shear, colder troposphere, and drier boundary layer all help TC intensification in the ENP; the atmospheric circulation tends to keep ENP hurricanes at relatively low latitudes for much of their lifetime, favoring strong low-level inflow and more confined ascent motion (Smith et al. 2015); maintaining a compact/small size during their intensification stage significantly increases the hurricanes' horizontal pressure gradient (Kilroy and Smith 2017; Hoarau et al. 2017) and sea spray effects. All these factors contribute toward faster intensification of ENP TCs (Fig. 9). These findings suggest that Hurricane Patricia became a record-breaking intense TC not only because of abnormally favorable thermal conditions associated

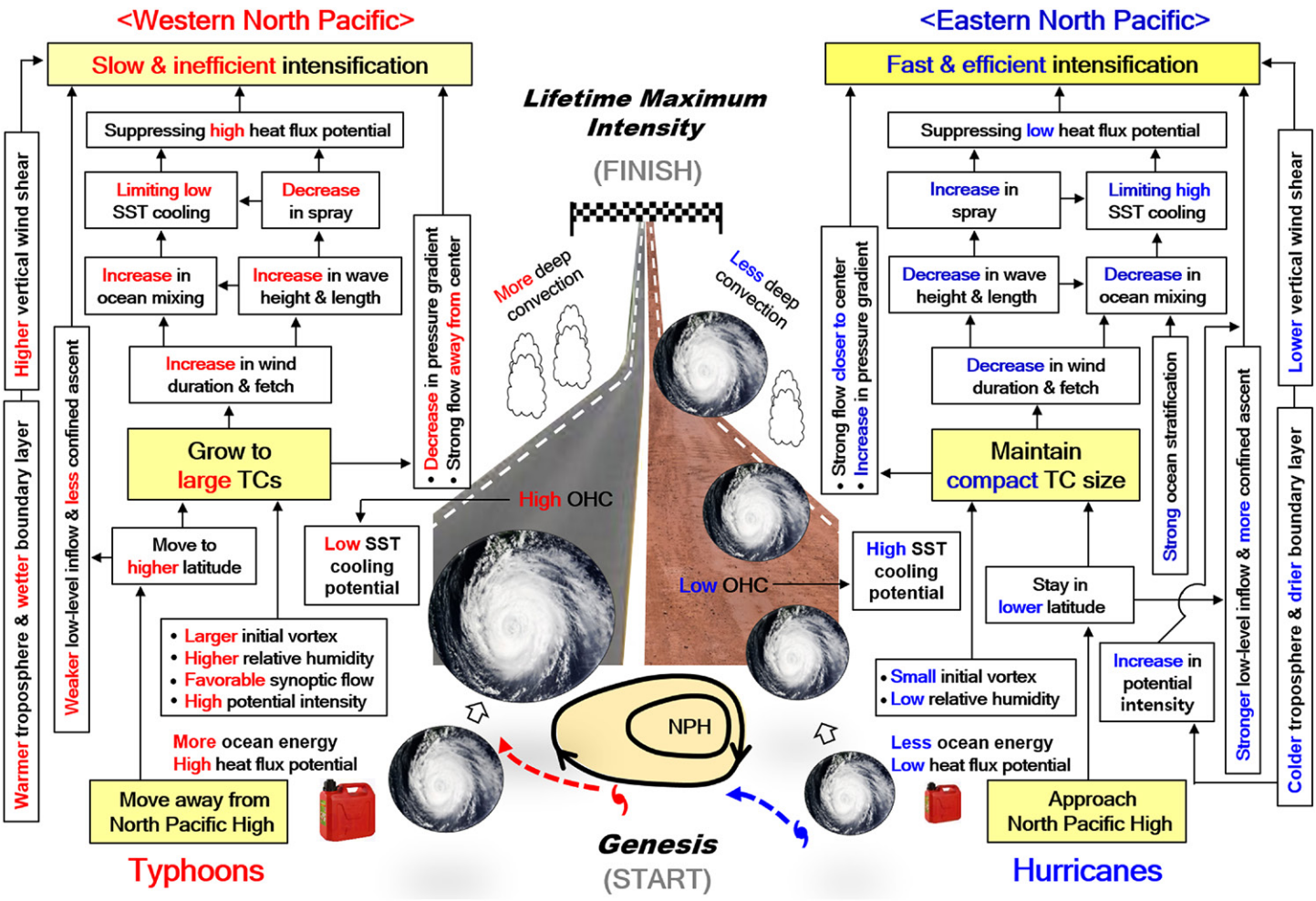

Fig. 9. Schematic of physical processes associated with the intensification efficiency of Pacific hurricanes and typhoons. Red and blue colors indicate characteristics of WPN typhoons and ENP hurricanes, respectively, and of the environments in the WNP and ENP, respectively. NPH represents the North Pacific high.

with the buildup of the strongest El Niño ever recorded (Huang et al. 2017) but also because of other large-scale environmental characteristics in the ENP, as reported in this study, resulting in an extreme RI event.

It should be noted that though ENP hurricanes intensify faster than WNP typhoons with a given ocean energy, their mean LMI is lower than that of WNP typhoons (Table 2), suggesting that their high IE does not seem to affect the final LMI. This may be related to the fact that the thermodynamic environmental support for higher LMIs, as represented by SST, OHC, and PI is, on average, greater in the WNP than in the ENP. A more detailed investigation of the basin-dependent relationship between LMI and IE remains a subject of future research.

One key factor influencing the basin dependence of TC intensification efficiency is related to whether TCs move away from or approach the region's subtropical highs, which depends on their location and the steering flow. TCs tend to move away from the subtropical highs in the WNP (see Fig. 2), moving into regions where the TC size increases more, the mean latitude of tracks is high, and thus the intensification efficiency tends to be low. In the ENP, the opposite occurs as the TCs tend to be steered along lower latitude tracks by the winds around the subtropical highs.

These findings on interbasin differences related to TC intensification highlight the importance of several factors, including TC size, latitude, subtropical ridges of high pressure, and ocean waves, some of which have not received much attention thus far in either TC intensity or in interpreting interbasin differences in TC intensification. Particularly, our modeling work and additional subsampling analyses point toward basin-dependent characteristics of TC size as significantly influencing TC intensity and IE through oceanic and air–sea interaction processes, emphasizing the importance of accurate TC size prediction (Landsea and Franklin 2013; Reul et al. 2017).

One concern is that current TC size prediction skills are very limited; even in a state-of-the-art operational TC prediction model—the Hurricane Weather Research and Forecast Model—it is reported that the mean prediction error percentages for 0–72-h lead times reach 60% for R64 (Pun et al. 2021). Inaccurate predictions of the TC size not only lead to SST cooling errors, but also influence deep convection and spinup processes that are crucial for TC intensification (Kilroy and Smith 2017; Pun et al. 2021), which in turn increases TC intensity prediction errors. In particular, TC size prediction may be more challenging in the ENP, with many compact hurricanes such as Patricia. This is because, at the spatial resolution of the current operational model (Biswas et al. 2018), it may be difficult for the model to accurately simulate important inner core TC structure, including the relatively small eyes of compact TCs. Simulated TC eye size has been shown to be sensitive to model resolution (Davis et al. 2008). Therefore, higher resolution models with physics and initialization schemes capable of simulating compact TC structures could be a way to improve TC intensity prediction in the ENP. Finally, our findings also emphasize that ocean wave coupling—an important missing link in most operating hurricane models—helps to account for the modulation of ocean mixing and sea spray depending on the TC size, which suggests another possible pathway for improving TC prediction skill.

Acknowledgments. We would like to offer special thanks to M. A. Donelan, although no longer with us, for helping this study, and Morris Bender and Kun Gao (Princeton University CIMES) for reviewing this paper and providing useful comments. This research was supported by Basic Science Research Program through the National Research Foundation of Korea (NRF) funded by the Ministry of Education (2021R1A2C1005287) and a part of the project titled "Establishment of the ocean research station in the jurisdiction zone and convergence research (20210607)" and "Study on Northwestern Pacific Warming and Genesis and Rapid Intensification of Typhoon (20220566)"

funded by the Ministry of Oceans and Fisheries, South Korea. We thank the anonymous reviewers for reading our manuscript carefully and providing many insightful comments and suggestions, which greatly improved the original manuscript. We also thank M. Y. Kim, S.-H. Kim, and C.-M. Ko for their assistance with the numerical experiments and analysis.

Data availability statement. The data that support the findings of this study are freely available to download from the URLs provided in appendix A, or from the corresponding author upon request. All codes used to analyze and plot the data are available from the corresponding author upon request.

Appendix A: Data

The best tracks of TCs were obtained from International Best Track Archive for Climate Stewardship (IBTrACS) version 4 during 2001–15, which contain estimates of the latitude, longitude, 1-min maximum sustained surface winds, central pressure, and radial extent (RMW, R34, R50, and R64) of maximum and 34-, 50-, and 64-kt winds in four quadrants. This study only uses data from the National Hurricane Center (NHC) and the Joint Typhoon Warning Center (JTWC), which both use a 1-min sustained wind. To compare axisymmetric TC sizes between basins, the radial extents are averaged using nonzero wind radii among the four quadrants. The lifetime maximum intensity (LMI) locations are where TCs reach LMI for the first time during their lifetime. Genesis is defined when a TC first reaches a tropical storm stage with the maximum wind speed (MWS) of 17 m s^{-1}.

The oceanic data for calculating SST, OHC, AOHC, and N^2 (in Tables 2 and 3) and for the numerical experiments (Fig. 4) were obtained from monthly mean ECCO-2 data (0.25° × 0.25°, https://ecco.jpl.nasa.gov/drive/files/ECCO2/cube92_latlon_quart_90S90N) and monthly NOAA Optimum Interpolation SST (OISST) version 2 (1° × 1°, https://www.esrl.noaa.gov/psd/data/gridded/data.noaa.oisst.v2.html). The atmospheric data for estimating VWS, IS, CAPE, SS, MSE, RH, T_a, and $q_s - q_a$ (in Table 3) were obtained from the monthly ERA-Interim reanalysis data (0.75° × 0.75°, https://www.ecmwf.int/en/forecasts/datasets/reanalysis-datasets/era-interim). For oceanic and atmospheric variables during the passages of Patricia and Haiyan (in Table 1 and Fig. 1) and variables using "during," "pre," and "T100" used throughout the paper, 3-day mean ECCO-2 and 6-h ERA-Interim reanalysis data are used. All atmospheric and oceanic metrics were averaged based on values derived from the mean environmental data obtained at locations along each storm track from the time of genesis to the LMI stage. The vertical wind shear (VWS) estimates for Haiyan and Patricia were done in the following order: (i) removing TC vortices using a filter based on Kurihara et al. (1993), (ii) calculating the magnitude of the difference between the 850- and 200-hPa wind vectors at each grid point, and (iii) area-averaging the values. All atmospheric (oceanic) variables are averaged within a 500-km (200-km) radius from the storm center along the TC tracks.

Appendix B: Storm-related parameters

The T_{req} is defined as the LMI-reaching time (T_{LMI}) from genesis per unit of the intensity change (10 m s^{-1} MWS). In this study, T_{req} was determined as the slope of a linear regression function, T_{LMI} = slope × (LMI − 17), in the scatterplot of Fig. 3a. Three IEs are defined as the ratio of intensity change achieved from the time of genesis to LMI per unit of accumulated OHC (AOHC), accumulated sea surface heat content (ASSHC), and accumulated air–sea enthalpy flux (AFLUX), respectively (see appendix C). For example, AOHC-based IE is determined as the slope of a linear regression function, LMI = slope × AOHC + 17, in the scatterplot of Fig. 3b. The other two IEs are also determined in the same way (Figs. 3c,d). The resident time (RT) of the TC is defined as a length scale of the TC size [specified as the radius of a 64-kt wind (R64)] (Pun et al. 2018) divided by translation speed (V_{storm}); the larger the RT is, the stronger the ocean mixing. The subscripts "pre" and "during" represent three days before the arrival

of the TC (i.e., pre-TC condition) and underneath the TC (i.e., when TC-induced SST cooling is considered), respectively.

Appendix C: Oceanic parameters

The AOHC is the summation of OHC from TC genesis to the time of first reaching the LMI:

$$\mathrm{AOHC} = \sum_{t=T_g}^{T_{\mathrm{LMI}}} \rho c_p \int_0^{\mathrm{d26}} T(z)\, dz, \tag{C1}$$

where $T(z)$ is the water temperature profile before the arrival of the TC (°C), c_p is the specific heat of seawater, d26 is the depth of 26°C isotherm, ρ is the water density, T_g is the genesis time (i.e., when TCs first achieve 17 m s^{-1} wind speed), and T_{LMI} is the time when a TC first reaches the LMI. Relative SST (R_{SST}) is calculated by dividing the SST at each grid by the tropical-mean SST (30°S–30°N) (Lin et al. 2015). The accumulated sea surface heat content ($\mathrm{ASSHC}_{\mathrm{during}}$) is similar to the AOHC but is calculated using the $\mathrm{SST}_{\mathrm{during}}$ instead of the OHC:

$$\mathrm{ASSHC}_{\mathrm{during}} = \sum_{t=T_g}^{T_{\mathrm{LMI}}} \rho c_p \mathrm{SST}_{\mathrm{during}}. \tag{C2}$$

The AOHC and $\mathrm{ASSHC}_{\mathrm{during}}$ values are averaged within the 200-km radius from the storm center to calculate the intensification efficiency.

$\mathrm{PI}_{\mathrm{pre}}$, $\mathrm{PI}_{\mathrm{T100}}$, and $\mathrm{PI}_{\mathrm{during}}$ are calculated using Emanuel's potential intensity code, which is available online (ftp://texmex.mit.edu/pub/emanuel/TCMAX/pcmin.m). $\mathrm{PI}_{\mathrm{pre}}$ is based on the SST before the arrival of the TC (i.e., $\mathrm{SST}_{\mathrm{pre}}$). $\mathrm{PI}_{\mathrm{T100}}$ and $\mathrm{PI}_{\mathrm{during}}$ attempt to include the effect of ocean cooling. The former uses the pre-TC depth-averaged ocean temperature (Lin et al. 2013) (i.e., temperature averaged from the surface down to the expected TC-induced mixing depth—100 m in this study, T_{100}) instead of $\mathrm{SST}_{\mathrm{pre}}$; the latter uses the SST underneath the TC ($\mathrm{SST}_{\mathrm{during}}$), which is calculated based on variable mixing depth instead of a fixed 100-m depth (see appendix D).

$$\mathrm{PI}_{\mathrm{SST}} = \frac{\mathrm{SST} - T_o}{T_o} \frac{C_k}{C_D}\left(k^* - k\right), \tag{C3}$$

$$\mathrm{PI}_{\mathrm{T100}} = \frac{T_{100} - T_o}{T_o} \frac{C_k}{C_D}\left(k^* - k\right), \tag{C4}$$

$$\mathrm{PI}_{\mathrm{during}} = \frac{\mathrm{SST}_{\mathrm{during}} - T_o}{T_o} \frac{C_k}{C_D}\left(k^* - k\right), \tag{C5}$$

where T_o is the TC outflow temperature; C_D and C_k are the drag coefficient and enthalpy exchange coefficients, respectively; k^* is the saturation enthalpy of the sea surface; and k is the surface enthalpy in the TC environment. For convenience in this study, $\mathrm{PI}_{\mathrm{pre}}$ is called the uncoupled potential intensity and $\mathrm{PI}_{\mathrm{during}}$ is the coupled potential intensity. The Brunt–Väisälä frequency (N^2) is defined as follows:

$$N^2 = \frac{g}{\rho}\frac{d\rho}{dz}, \tag{C6}$$

where ρ is the potential density that depends on both temperature and salinity, and g is the gravitational acceleration (9.8 m s^{-2}). The maximum N^2 is the largest value at each profile.

Air–sea enthalpy flux is the sum of sensible heat flux (SHF) and latent heat flux (LHF). The bulk formulas for SHF and LHF calculations are

$$\mathrm{SHF} = C_H W\left(T_s - T_a\right)\rho_a Cp_a, \tag{C7}$$

$$\mathrm{LHF} = C_H W\left(q_s - q_a\right)\rho_a L\upsilon_a, \tag{C8}$$

where C_H and C_E are the sensible and latent heat exchange coefficients under high wind condition, which are defined as 1.1×10^{-3} and 1.2×10^{-3}, respectively (Lin et al. 2021). The terms W, ρ_a, Cp_a, and $L\upsilon_a$ are maximum wind speed (1-min sustained wind from JTWC), air density, heat capacity of the air (~1005 J kg^{-1} K^{-1}), and latent heat of vaporization (~2.5×10^6 J kg^{-1}), respectively. The terms T_s, T_a, q_s, and q_a are $\mathrm{SST}_{\mathrm{during}}$, near-surface air temperature, the saturation specific humidity at the $\mathrm{SST}_{\mathrm{during}}$, and the specific humidity of near-surface air, respectively.

Appendix D: Estimation of SST cooling underneath the TC

In this study, the SST underneath the TC ($\mathrm{SST}_{\mathrm{during}}$), which considers TC-induced SST cooling effect, was calculated based on the variable depth of Price (2009). The variable depth (d) is parameterized to account for vertical turbulent mixing in the upper ocean with the hurricane forcing. The parameterization assumes that the bulk Richardson number of the surface mixed layer should not be less than a critical value (0.6) (Price 1981),

$$\frac{g\left[\rho\left(z=-d\right) - \dfrac{-1}{d}\displaystyle\int_0^{-d}\rho\left(z\right)dz\right]d}{\rho_o\left(\dfrac{\tau}{\rho_o d}\dfrac{4R_h}{V_{\mathrm{storm}}}S\right)^2} \geq 0.6, \tag{D1}$$

where g is the acceleration of gravity, $\rho(z)$ is the water density profile, z is the water depth, τ is the wind stress, R_h/V_{storm} is the TC residence time (RT; R_h, the TC size; V_{storm}, storm translation speed), and S is a constant ($S = 1.2$) (Price 2009). $\mathrm{SST}_{\mathrm{during}}$ is then calculated by averaging pre-TC (3 days before TC's arrival) ocean temperature profile from the surface down to the estimated variable depth.

This simple method is generally less accurate than 3D numerical ocean model solutions, but it may be useful for the purpose of comparative analysis of the factors determining the magnitude of TC-induced SST cooling between ENP and WNP. For example, the storm translation speed in Eq. (D1) is on average slower in the ENP (4.6 m s^{-1}) than in the WNP (5.0 m s^{-1}) (see V_{storm} in Table 3), which can enhance the SST cooling in the ENP. However, when both storm translation speed and TC size affecting SST cooling are considered (cf. the residence time, RT, of two basins in Table 3), ENP hurricanes produce less SST cooling than WNP typhoons do under the same oceanic conditions because of the greater fractional difference in TC size than in storm translation speed between the two basins. The density profile, $\rho(z)$, in Eq. (D1) also explains the reduction in vertical mixing in the ENP with a larger Brunt–Väisälä frequency (N^2).

Appendix E: Numerical experiments

To investigate the effect of TC size and wave-induced mixing on SST cooling (Figs. 4–6), a series of ideal numerical experiments were conducted using the Regional Oceanic Modeling

System (ROMS, version 3.6, 1/12° × 1/12°, 30 vertical layers) (Shchepetkin and McWilliams 2005) and WAVEWATCH III (WW3, version 5.16, 1/12° × 1/12°, 25 frequencies extending from 0.0418 to 0.3058 Hz) (WW3DG 2016). In these experiments, two idealized steady-moving symmetric TCs with different sizes were used, in which the maximum wind speed was fixed at 60 m s^{-1} and the translation speed was set to 5 m s^{-1} (Figs. 4a,e). The wind fields for these experiments were obtained from an analytical model based on Moon et al. (2003). The model requires the maximum wind speed and its radius, the radii of wind speeds of 18 and 26 m s^{-1} in all four quadrants of the TC, as well as the central pressure and location of the TC center. These storm parameters were first interpolated in time to the model time step (30 min). The radial wind profiles were then calculated along the northeast, southeast, northwest, and southwest directions, correspondingly. The two-dimensional wind field was generated by the spatial interpolation of the above radial profiles azimuthally. In these experiments, the radii were obtained from the mean LMI values in the ENP and WNP (Table 3). The initial conditions of ROMS were spatially uniform and obtained by averaging the *T*/*S* profiles for all TC points from July to October 2001–15.

The ocean mixing parameterization in this study was based on the k–ε one-dimensional mixing scheme (Rodi 1987). The k–ε scheme calculates the competing effects of the turbulent kinetic energy (k) versus the dissipation of that energy, thus calculating an approximation to the turbulent viscosity that determines the turbulent mixing. To examine the effect of wave-induced mixing on SST cooling, additional experiments considering ocean mixing due to nonbreaking waves were conducted. In this study, the wave-induced mixing was included as an additional term in the turbulent kinetic energy production based on Babanin and Haus (2009) and Aijaz et al. (2017), which assumes that all energy dissipated by nonbreaking waves goes into turbulence production. The turbulence production P_w is given by the following equation (Ghantous and Babanin 2014a,b):

$$P_W = b_1 k\omega^3 \frac{H^3}{8} e^{3kz}. \tag{E1}$$

where z is the water depth (positive upward), k is the wavenumber, ω is the radian frequency, and b_1 is a nondimensional proportionality constant (here specified as 0.0014) (Young et al. 2013); H is the significant wave height, which is calculated from WAVEWATCH III.

Appendix F: Atmospheric parameters

Vertical wind shear (VWS) is defined by the magnitude of the vector difference between 200- and 850-hPa winds:

$$\mathrm{VWS} = \sqrt{\left(U_{200} - U_{850}\right)^2 + \left(V_{200} - V_{850}\right)^2}, \tag{F1}$$

where U_{200} (V_{200}) is the 200-hPa zonal (meridional) wind and U_{850} (V_{850}) is the 850-hPa zonal (meridional) wind. Static stability (SS) is calculated as follows:

$$\mathrm{SS} = \frac{g}{\theta}\frac{\partial\theta}{\partial z}, \tag{F2}$$

where θ is the potential temperature. Convective available potential energy (CAPE) is calculated using the definition of the environmental CAPE of Emanuel's potential intensity code. Moisture static energy (MSE) is defined as follows:

$$\mathrm{MSE} = C_p T_a + gz + L_v q_v, \tag{F3}$$

where C_p is the specific heat of air at constant pressure (1004 J kg^{-1} K), T_a is the air temperature, g is gravitational acceleration, z is geopotential height, L_v is the latent heat of vaporization (2.5×10^6 J kg^{-1}), and q_v is specific humidity. The terms C_pT_a and L_vq_v are sensible heating and latent heating energy, respectively, and gz is potential energy. Inertial stability (IS) is approximately defined as

$$\mathrm{IS}^2 \approx f^2, \tag{F4}$$

where f is the Coriolis parameter. This definition does not include the effect of the cyclonic circulation in a TC (Wada et al. 2012). Relative humidity is an average between 500 and 700 hPa.

Appendix G: Factors affecting TC size

TC size is known to be affected by a number of factors: (i) synoptic flow pattern (Liu and Chan 2002) (the relatively smaller TCs in the ENP frequently form from an easterly wave synoptic pattern and are more influenced by the subtropical high during intensification, being embedded in the strong easterly trades of the subtropical ridge, while medium to large TCs in the WNP tend to form from the monsoon-related formation patterns and are associated with the northeasterly winter monsoon flow and southeasterly flow associated with the subtropical ridge); (ii) initial TC (or vortex) size (Chan and Chan 2014; Kilroy and Smith 2017; Xu and Wang 2010) (an initially larger TC generally has a larger size at later stage); (iii) average latitude of TC occurrence (Chan and Chan 2013; Chavas and Reed 2019; Lee et al. 2010) (TC size generally increases with latitude); and (iv) environmental relative humidity (Hill and Lackmann 2009; Wang 2012; Xu and Wang 2010) and SST (Chavas et al. 2016; Lin et al. 2015) (larger TC size is related to higher TC environmental relative humidity and SST). Average TC size differences between the ENP and WNP may be related to these factors. The mean initial disturbance size R34 (R_{init}) values are ~9% larger for the WNP than ENP (see Table 3). Other beneficial conditions in the WNP for increasing TC size include high relative SST (see R_{SST} in Table 2), favorable synoptic flow patterns for development (Lee et al. 2010), monsoonal environment with higher tropospheric relative humidity (see RH in Table 3), and higher average latitude of TC occurrence (see LAT in Table 3). These conditions may be related to whether TCs move away from or approach the region's subtropical highs. For example, in the ENP, hurricanes approach the North Pacific high or the high pressure system located in Mexico during the summer (Wood and Ritchie 2015) (Fig. 2a). If they are approaching the North Pacific high, the steering winds tend to keep the storm at a relatively low latitude, where it is more likely to remain relatively small. We speculate that storms in the ENP approaching the subtropical ridge may also maintain a smaller size because of interaction with the ridge itself (Weatherford and Gray 1988). In the WNP, typhoons move around the southwestern edge of the North Pacific high or head toward more favorable environments for TC size growth (higher latitude, monsoonal environment with higher tropospheric relative humidity) away from the North Pacific high. For the particular case of Haiyan versus Patricia, we speculate that the difference in their size is mainly due to whether TCs move away from or approach the subtropical ridge. The fact that the mean ambient surface pressure during the intensification of Patricia (1007.8 ± 0.9 hPa) was significantly higher than that of Haiyan (1005.9 ± 1.5 hPa) may support this hypothesis. In terms of simulating TC size differences between the ENP and WNP, at least one dynamical downscaling climate modeling framework (Knutson et al. 2015) simulates a fairly realistic interbasin variation of climatological TC sizes, with the smallest (largest) TCs simulated in the ENP (WNP) basin, although ENP sizes are biased high in the model.

References

Aijaz, S., M. Ghantous, A. V. Babanin, I. Ginis, B. Thomas, and G. Wake, 2017: Nonbreaking wave-induced mixing in upper ocean during tropical cyclones using coupled hurricane-ocean-wave modeling. *J. Geophys. Res. Oceans*, **122**, 3939–3963, https://doi.org/10.1002/2016JC012219.

Andreas, E. L, and K. A. Emanuel, 2001: Effects of sea spray on tropical cyclone intensity. *J. Atmos. Sci.*, **58**, 3741–3751, https://doi.org/10.1175/1520-0469(2001)058<3741:EOSSOT>2.0.CO;2.

Babanin, A. V., 2006: On a wave-induced turbulence and a wave-mixed upper ocean layer. *Geophys. Res. Lett.*, **33**, L20605, https://doi.org/10.1029/2006GL027308.

——, and B. K. Haus, 2009: On the existence of water turbulence induced by nonbreaking surface waves. *J. Phys. Oceanogr.*, **39**, 2675–2679, https://doi.org/10.1175/2009JPO4202.1.

Bao, J. W., C. W. Fairall, S. A. Michelson, and L. Bianco, 2011: Parameterizations of sea-spray impact on the air–sea momentum and heat fluxes. *Mon. Wea. Rev.*, **139**, 3781–3797, https://doi.org/10.1175/MWR-D-11-00007.1.

Biswas, M. K., and Coauthors, 2018: Hurricane Weather Research and Forecasting (HWRF) Model: 2017 scientific documentation. NCAR Tech. Note NCAR/TN-544+STR, 99 pp., https://doi.org/10.5065/D6MK6BPR.

Carrasco, C. A., C. W. Landsea, and Y. L. Lin, 2014: The influence of tropical cyclone size on its intensification. *Wea. Forecasting*, **29**, 582–590, https://doi.org/10.1175/WAF-D-13-00092.1.

Chan, K. T., and J. C. L. Chan, 2013: Angular momentum transports and synoptic flow patterns associated with tropical cyclone size change. *Mon. Wea. Rev.*, **141**, 3985–4007, https://doi.org/10.1175/MWR-D-12-00204.1.

——, and ——, 2014: Impacts of initial vortex size and planetary vorticity on tropical cyclone size. *Quart. J. Roy. Meteor. Soc.*, **140**, 2235–2248, https://doi.org/10.1002/qj.2292.

Chavas, D. R., and K. A. Reed, 2019: Dynamical aquaplanet experiments with uniform thermal forcing: System dynamics and implications for tropical cyclone genesis and size. *J. Atmos. Sci.*, **76**, 2257–2274, https://doi.org/10.1175/JAS-D-19-0001.1.

——, N. Lin, W. Dong, and Y. Lin, 2016: Observed tropical cyclone size revisited. *J. Climate*, **29**, 2923–2939, https://doi.org/10.1175/JCLI-D-15-0731.1.

Cione, J. J., and E. W. Uhlhorn, 2003: Sea surface temperature variability in hurricanes: Implications with respect to intensity change. *Mon. Wea. Rev.*, **131**, 1783–1796, https://doi.org/10.1175//2562.1.

Davis, C. A., and Coauthors, 2008: Prediction of land falling hurricanes with the Advanced Hurricane WRF model. *Mon. Wea. Rev.*, **136**, 1990–2005, https://doi.org/10.1175/2007MWR2085.1.

DeMaria, M., and J. Kaplan, 1994: A Statistical Hurricane Intensity Prediction Scheme (SHIPS) for the Atlantic Basin. *Wea. Forecasting*, **9**, 209–220, https://doi.org/10.1175/1520-0434(1994)009<0209:ASHIPS>2.0.CO;2.

——, M. Mainelli, L. K. Shay, J. A. Knaff, and J. Kaplan, 2005: Further improvements to the Statistical Hurricane Intensity Prediction Scheme (SHIPS). *Wea. Forecasting*, **20**, 531–543, https://doi.org/10.1175/WAF862.1.

Elsberry, R. L., L. Chen, J. Davidson, R. Rogers, Y. Wang, and L. Wu, 2013: Advances in understanding and forecasting rapidly changing phenomena in tropical cyclones. *Trop. Cyclone Res. Rev.*, **2**, 13–24, https://doi.org/10.6057/2013TCRR01.02.

Emanuel, K. A., 1991: The theory of hurricanes. *Annu. Rev. Fluid Mech.*, **23**, 179–196, https://doi.org/10.1146/annurev.fl.23.010191.001143.

——, 1999: Thermodynamic control of hurricane intensity. *Nature*, **401**, 665–669, https://doi.org/10.1038/44326.

Foltz, G. R., and K. Balaguru, 2016: Prolonged El Niño conditions in 2014–2015 and the rapid intensification of Hurricane Patricia in the eastern Pacific. *Geophys. Res. Lett.*, **43**, 10 347–10 355, https://doi.org/10.1002/2016GL070274.

——, ——, and S. Hagos, 2018: Interbasin differences in the relationship between SST and tropical cyclone intensification. *Mon. Wea. Rev.*, **146**, 853–870, https://doi.org/10.1175/MWR-D-17-0155.1.

Ghantous, M., and A. V. Babanin, 2014a: One-dimensional modelling of upper ocean mixing by turbulence due to wave orbital motion. *Nonlinear Processes Geophys.*, **21**, 325–338, https://doi.org/10.5194/npg-21-325-2014.

——, and ——, 2014b: Ocean mixing by wave orbital motion. *Acta Phys. Slovaca*, **64** (1), 1–57.

Hill, K. A., and G. M. Lackmann, 2009: Influence of environmental humidity on tropical cyclone size. *Mon. Wea. Rev.*, **137**, 3294–3315, https://doi.org/10.1175/2009MWR2679.1.

Hoarau, K., L. Mark, G. Rosalina, G. Chip, and B. Rose, 2017: Did Typhoon Haiyan have a new record-minimum pressure? *Weather*, **72**, 291–295, https://doi.org/10.1002/wea.3045.

Holland, G. I., and R. T. Merrill, 1984: On the dynamics of tropical cyclone structural changes. *Quart. J. Roy. Meteor. Soc.*, **110**, 723–745, https://doi.org/10.1002/qj.49711046510.

Huang, H. C., J. Boucharel, I. I. Lin, F. F. Jin, C. C. Lien, and I. F. Pun, 2017: Air-sea fluxes for Hurricane Patricia (2015): Comparison with Supertyphoon Haiyan (2013) and under different ENSO conditions. *J. Geophys. Res. Oceans*, **122**, 6076–6089, https://doi.org/10.1002/2017JC012741.

Johnson, G. C., S. Schmidtko, and J. M. Lyman, 2012: Relative contributions of temperature and salinity to seasonal mixed layer density changes and horizontal density gradients. *J. Geophys. Res.*, **117**, C04015, https://doi.org/10.1029/2011JC007651.

Kaplan, J., and M. DeMaria, 2003: Large-scale characteristics of rapidly intensifying tropical cyclones in the North Atlantic basin. *Wea. Forecasting*, **18**, 1093–1108, https://doi.org/10.1175/1520-0434(2003)018<1093:LCORIT>2.0.CO;2.

——, ——, and J. A. Knaff, 2010: A revised tropical cyclone rapid intensification index for the Atlantic and eastern North Pacific basins. *Wea. Forecasting*, **25**, 220–241, https://doi.org/10.1175/2009WAF2222280.1.

Kilroy, G., and R. K. Smith, 2017: The effects of initial vortex size on tropical cyclogenesis and intensification. *Quart. J. Roy. Meteor. Soc.*, **143**, 2832–2845, https://doi.org/10.1002/qj.3134.

Kim, S. H., I. J. Moon, and P. S. Chu, 2018: Statistical-dynamical typhoon intensity predictions in the western North Pacific using track pattern clustering and ocean coupling predictors. *Wea. Forecasting*, **33**, 347–365, https://doi.org/10.1175/WAF-D-17-0082.1.

Kimberlain, T. B., E. S., Blake, and J. P. Cangialosi, 2016: Hurricane Patricia (EP202015). National Hurricane Center Tropical Cyclone Rep., 32 pp., https://www.nhc.noaa.gov/data/tcr/EP202015_Patricia.pdf.

Knaff, J., and R. M. Zehr, 2007: Reexamination of tropical cyclone wind–pressure relationships. *Wea. Forecasting*, **22**, 71–88, https://doi.org/10.1175/WAF965.1.

Knutson, T. R., J. J. Sirutis, M. Zhao, R. E. Tuleya, M. Bender, G. A. Vecchi, G. Villarini, and D. Chavas, 2015: Global projections of intense tropical cyclone activity for the late twenty-first century from dynamical downscaling of CMIP5/RCP4.5 scenarios. *J. Climate*, **28**, 7203–7224, https://doi.org/10.1175/JCLI-D-15-0129.1.

Kurihara, Y., M. A. Bender, and R. J. Ross, 1993: An initialization scheme of hurricane models by vortex specification. *Mon. Wea. Rev.*, **121**, 2030–2045, https://doi.org/10.1175/1520-0493(1993)121<2030:AISOHM>2.0.CO;2.

Landsea, C. W., and J. L. Franklin, 2013: Atlantic Hurricane Database uncertainty and presentation of a new database format. *Mon. Wea. Rev.*, **141**, 3576–3592, https://doi.org/10.1175/MWR-D-12-00254.1.

Lee, C.-S., K. K. W. Cheung, W. T. Fang, and R. L. Elsberry, 2010: Initial maintenance of tropical cyclone size in the western North Pacific. *Mon. Wea. Rev.*, **138**, 3207–3223, https://doi.org/10.1175/2010MWR3023.1.

Leipper, D. F., and D. Volgenau, 1972: Hurricane heat potential of the Gulf of Mexico. *J. Phys. Oceanogr.*, **2**, 218–224, https://doi.org/10.1175/1520-0485(1972)002<0218:HHPOTG>2.0.CO;2.

Li, T., X. Ge, M. Peng, and W. Wang, 2012: Dependence of tropical cyclone intensification on the Coriolis parameter. *Trop. Cyclone Res. Rev.*, **1**, 242–253, https://doi.org/10.6057/2012TCRR02.04.

Lin, I. I., C. C. Wu, I. F. Pun, and D. S. Ko, 2008: Upper-ocean thermal structure and the western North Pacific category 5 typhoons. Part I: Ocean features and the category 5 typhoons' intensification. *Mon. Wea. Rev.*, **136**, 3288–3306, https://doi.org/10.1175/2008MWR2277.1.

——, I. F. Pun, and C. C. Wu, 2009: Upper-ocean thermal structure and the western North Pacific category 5 typhoons. Part II: Dependence on translation speed. *Mon. Wea. Rev.*, **137**, 3744–3757, https://doi.org/10.1175/2009MWR2713.1.

——, and Coauthors, 2013: An ocean coupling potential intensity index for tropical cyclones. *Geophys. Res. Lett.*, **40**, 1878–1882, https://doi.org/10.1002/grl.50091.

——, and Coauthors, 2021: A tale of two rapidly intensifying supertyphoons: Hagibis (2019) and Haiyan (2013). *Bull. Amer. Meteor*, **102**, E1645–E1644, https://doi.org/10.1175/BAMS-D-20-0223.1.

Lin, Y., M. Zhao, and M. Zhang, 2015: Tropical cyclone rainfall area controlled by relative sea surface temperature. *Nat. Commun.*, **6**, 6591, https://doi.org/10.1038/ncomms7591.

Liu, K. S., and J. C. L. Chan, 2002: Synoptic flow patterns associated with small and large tropical cyclones over the western North Pacific. *Mon. Wea. Rev.*, **130**, 2134–2142, https://doi.org/10.1175/1520-0493(2002)130<2134:SFPAWS>2.0.CO;2.

Lovelock, J. E., 2003: Gaia: The living Earth. *Nature*, **426**, 769–770, https://doi.org/10.1038/426769a.

Mainelli, M., M. DeMaria, L. K. Shay, and G. Goni, 2008: Application of oceanic heat content estimation to operational forecasting of recent Atlantic category 5 hurricanes. *Wea. Forecasting*, **23**, 3–16, https://doi.org/10.1175/2007WAF2006111.1.

Merrill, R. T., 1988: Environmental influences on hurricane intensification. *J. Atmos. Sci.*, **45**, 1678–1687, https://doi.org/10.1175/1520-0469(1988)045<1678:EIOHI>2.0.CO;2.

Moon, I. J., and S. J. Kwon, 2012: Impact of upper-ocean thermal structure on the intensity of Korean peninsula landfall typhoons. *Prog. Oceanogr.*, **105**, 61–66, https://doi.org/10.1016/j.pocean.2012.04.008.

——, I. Ginis, T. Hara, H. L. Tolman, C. W. Wright, and E. J. Walsh, 2003: Numerical simulation of sea surface directional wave spectra under hurricane wind forcing. *J. Phys. Oceanogr.*, **33**, 1680–1706, https://doi.org/10.1175/2410.1.

——, ——, and ——, 2004: Effect of surface waves on air–sea momentum exchange: II. Behavior of drag coefficient under tropical cyclones. *J. Atmos. Sci.*, **61**, 2334–2348, https://doi.org/10.1175/1520-0469(2004)061<2334:EOSWOA>2.0.CO;2.

Mori, N., M. Kato, S. Kim, H. Mase, Y. Shibutani, T. Takemi, K. Tsuboki, and T. Yasuda, 2014: Local amplification of storm surge by Super Typhoon Haiyan in Leyte Gulf. *Geophys. Res. Lett.*, **41**, 5106–5113, https://doi.org/10.1002/2014GL060689.

Price, J. F., 1981: Upper ocean response to a hurricane. *J. Phys. Oceanogr.*, **11**, 153–175, https://doi.org/10.1175/1520-0485(1981)011<0153:UORTAH>2.0.CO;2.

——, 2009: Metrics of hurricane-ocean interaction: Vertically-integrated or vertically-averaged ocean temperature? *Ocean Sci.*, **5**, 351–368, https://doi.org/10.5194/os-5-351-2009.

Pun, I. F., I. I. Lin, C. C. Lien, and C. C. Wu, 2018: Influence of the size of Supertyphoon Megi (2010) on SST cooling. *Mon. Wea. Rev.*, **146**, 661–677, https://doi.org/10.1175/MWR-D-17-0044.1.

——, J. A. Knaff, and C. R. Sampson, 2021: Uncertainty of tropical cyclone wind radii on sea surface temperature cooling. *J. Geophys. Res. Atmos.*, **126**, e2021JD034857, https://doi.org/10.1029/2021JD034857.

Reul, N., and Coauthors, 2017: A new generation of tropical cyclone size measurements from space. *Bull. Amer. Meteor. Soc.*, **98**, 2367–2385, https://doi.org/10.1175/BAMS-D-15-00291.1.

Rodi, W., 1987: Examples of calculation methods for flow and mixing in stratified flows. *J. Geophys. Res.*, **92**, 5305–5328, https://doi.org/10.1029/JC092iC05p05305.

Rogers, R. F., and Coauthors, 2017: Rewriting the tropical record books: The extraordinary intensification of Hurricane Patricia (2015). *Bull. Amer. Meteor. Soc.*, **98**, 2091–2112, https://doi.org/10.1175/BAMS-D-16-0039.1.

Shay, L. K., and J. K. Brewster, 2010: Oceanic heat content variability in the eastern Pacific Ocean for hurricane intensity forecasting. *Mon. Wea. Rev.*, **138**, 2110–2131, https://doi.org/10.1175/2010MWR3189.1.

——, G. J. Goni, and P. G. Black, 2000: Role of a warm ocean feature on Hurricane Opal. *Mon. Wea. Rev.*, **128**, 1366–1383, https://doi.org/10.1175/1520-0493(2000)128<1366:EOAWOF>2.0.CO;2.

Shchepetkin, A., and J. C. McWilliams, 2005: The Regional Oceanic Modeling System (ROMS): A split-explicit, free-surface, topography-following-coordinate ocean model. *Ocean Modell.*, **9**, 347–404, https://doi.org/10.1016/j.ocemod.2004.08.002.

Smith, R. K., G. Kilroy, and M. T. Montgomery, 2015: Why do model tropical cyclones intensify more rapidly at low latitudes? *J. Atmos. Sci.*, **72**, 1783–1804, https://doi.org/10.1175/JAS-D-14-0044.1.

Stoney, L., K. Walsh, A. V. Babanin, M. Ghantous, P. Govekar, and I. Young, 2017: Simulated ocean response to tropical cyclones: The effect of a novel parameterization of mixing from unbroken surface waves. *J. Adv. Model. Earth Syst.*, **9**, 759–780, https://doi.org/10.1002/2016MS000878.

Tao, D., and F. Zhang, 2015: Effects of vertical wind shear on the predictability of tropical cyclones: Practical versus intrinsic limit. *J. Adv. Model. Earth Syst.*, **7**, 1534–1553, https://doi.org/10.1002/2015MS000474.

Tory, K. J., and R. A. Dare, 2015: Sea surface temperature thresholds for tropical cyclone formation. *J. Climate*, **28**, 8171–8183, https://doi.org/10.1175/JCLI-D-14-00637.1.

Wada, A., and N. Usui, 2007: Importance of tropical cyclone heat potential for tropical cyclone intensity and intensification in the western North Pacific. *J. Oceanogr.*, **63**, 427–447, https://doi.org/10.1007/s10872-007-0039-0.

——, ——, and K. Sato, 2012: Relationship of maximum tropical cyclone intensity to sea surface temperature and tropical cyclone heat potential in the North Pacific Ocean. *J. Geophys. Res.*, **117**, D11118, https://doi.org/10.1029/2012JD017583.

——, S. Kanada, and H. Yamada, 2018: Effect of air–sea environmental conditions and interfacial processes on extremely intense Typhoon Haiyan (2013). *J. Geophys. Res. Atmos.*, **123**, 10 379–10 405, https://doi.org/10.1029/2017JD028139.

Walsh, K., P. Govekar, A. V. Babanin, M. Ghantous, P. Spence, and E. Scoccimarro, 2017: The effect on simulated ocean climate of a parameterization of unbroken wave-induced mixing incorporated into the k-epsilon mixing scheme. *J. Adv. Model. Earth Syst.*, **9**, 735–758, https://doi.org/10.1002/2016MS000707.

Wang, Y., 2012: Recent research progress on tropical cyclone structure and intensity. *Trop. Cyclone Res. Rev.*, **1**, 254–275, https://doi.org/10.6057/2012TCRR02.05.

——, J. D. Kepert, and G. J. Holland, 2001: The effect of sea spray evaporation on tropical cyclone boundary layer structure and intensity. *Mon. Wea. Rev.*, **129**, 2481–2500, https://doi.org/10.1175/1520-0493(2001)129<2481:TEOSSE>2.0.CO;2.

Weatherford, C. L., and W. M. Gray, 1988: Typhoon structure as revealed by aircraft reconnaissance. Part I: Data analysis and climatology. *Mon. Wea. Rev.*, **116**, 1032–1043, https://doi.org/10.1175/1520-0493(1988)116<1032:TSARBA>2.0.CO;2.

Wing, A. A., K. Emanuel, and S. Solomon, 2015: On the factors affecting trends and variability in tropical cyclone potential intensity. *Geophys. Res. Lett.*, **42**, 8669–8677, https://doi.org/10.1002/2015GL066145.

Wood, K. M., and E. A. Ritchie, 2015: A definition for rapid weakening of North Atlantic and eastern North Pacific tropical cyclones. *Geophys. Res. Lett.*, **42**, 10 091–10 097, https://doi.org/10.1002/2015GL066697.

Wu, L., and Coauthors, 2012: Relationship of environmental relative humidity with North Atlantic tropical cyclone intensity and intensification rate. *Geophys. Res. Lett.*, **39**, L20809, https://doi.org/10.1029/2012GL053546.

WW3DG, 2016: User manual and system documentation of WAVEWATCH III version 5.16. Tech. Note 329, NOAA/NWS/NCEP/MMAB, 326 pp., https://polar.ncep.noaa.gov/waves/wavewatch/manual.v5.16.pdf.

Xu, J., and Y. Wang, 2010: Sensitivity of the simulated tropical cyclone inner-core size to the initial vortex size. *Mon. Wea. Rev.*, **138**, 4135–4157, https://doi.org/10.1175/2010MWR3335.1.

——, ——, and C. Yang, 2019: Factors affecting the variability of maximum potential intensity (MPI) of tropical cyclones over the North Atlantic. *J. Geophys. Res. Atmos.*, **124**, 6654–6668, https://doi.org/10.1029/2019JD030283.

Xu, X., J. J. Voermans, H. Ma, C. Guan, and A. V. Babanin, 2021a: A wind-wave-dependent sea spray volume flux model based on field experiments. *J. Mar. Sci. Eng.*, **9**, 1168, https://doi.org/10.3390/jmse9111168.

——, ——, Q. Liu, I.-J. Moon, C. Guan, and A. V. Babanin, 2021b: Impacts of the wave-dependent sea spray parameterizations on air–sea–wave coupled modeling under an idealized tropical cyclone. *J. Mar. Sci. Eng.*, **9**, 1390, https://doi.org/10.3390/jmse9121390.

Young, I. R., 2017: A review of parametric descriptions of tropical cyclone wind-wave generation. *Atmosphere*, **8**, 194, https://doi.org/10.3390/atmos8100194.

——, A. V. Babanin, and S. Zieger, 2013: The decay rate of ocean swell observed by altimeter. *J. Phys. Oceanogr.*, **43**, 2322–2333, https://doi.org/10.1175/JPO-D-13-083.1.